ACS Catalysis

pubs.acs.org/acscatalysis

Research Article

Modified Adsorption Energies on Single-Layer IrO_2 and RuO_2 Films of IrO_2−RuO_2 Heterostructures: Localized Effect of Subsurface Metal−Oxygen Ligands

Suriya Ramasubramanian, Jisu Shin, Christopher J. Lee, Chethana Sudarshan, Omar Almarshad, Alvaro Loaiza Orduz, Randall J. Meyer, Craig Plaisance,* David Hibbitts,* and Jason F. Weaver*

Cite This: *ACS Catal.* 2025, 15, 11134−11149

Read Online

ACCESS | Metrics & More | Article Recommendations | Supporting Information

ABSTRACT: Rutile oxides offer a promising platform for creating and studying mixed metal oxide surfaces for catalytic applications. RuO_2 and IrO_2 have been used for the electrochemical oxygen evolution reaction and alkane oxidation reactions, and they have similar lattices which promotes the synthesis of layered structures (e.g., IrO_2/RuO_2) and IrO_2−RuO_2 solid solutions. Their low-energy surfaces, the (110) plane, expose rows of coordinatively unsaturated metal atoms (M_{cus}) which act as binding sites during catalysis. Here, we generated single-layer IrO_2 films on RuO_2(110), single-layer RuO_2 films on IrO_2(110), and their thick-film counterparts, and studied their binding properties using molecular N_2 and dissociative O_2 adsorption. Temperature-programmed desorption measurements and complementary density functional theory calculations and electronic structure analysis show that the binding properties of M_{cus} sites are strongly influenced by the identity of cations in the subsurface beneath the binding site (M_{subcus}), such that M_{subcus} identity influences binding as much as the identity of the M_{cus} binding site itself. Our analysis shows that these strong effects of the subsurface cations originate from localization of the σ system involved in adsorbate binding, and the resultant accumulation of charge on the subsurface O atom beneath the M_{cus} site upon adsorbate binding. Replacing Ru with Ir at the subsurface sites stabilizes this charge and strengthens the binding of both N_2 and O with the M_{cus} site. We discuss a computational alchemy model that can explain both the site and ligand effects of chemical binding on IrO_2/RuO_2 heterostructures and is extendable to other mixed metal oxide and metal alloy surfaces.

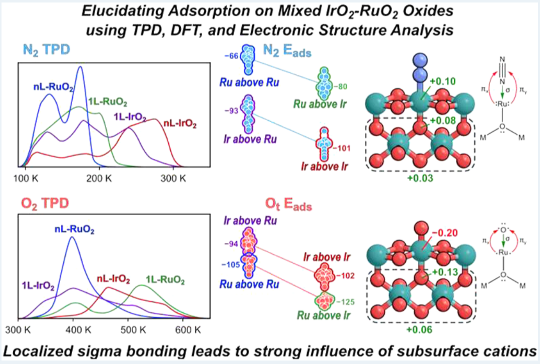

KEYWORDS: *IrO_2, RuO_2, rutile oxide, adsorption, ligand effect, computational alchemy, electronic structure analysis, mixed metal oxide*

INTRODUCTION

Combining different materials is a widely used strategy for modifying surface chemical properties and optimizing the use of precious metals in solid catalysts. For example, single-atom alloys involve the dispersion of chemically reactive precious metals (e.g., Pt, Rh, Pd) throughout less reactive coinage metals to reduce precious metal usage and generate isolated surface sites that can provide desirable catalytic properties distinct from those of pure precious metals.[1−3] Core−shell structures, often covering an earth-abundant metal with a monolayer of catalytically active metal (e.g., Pt/W), can also minimize precious metal usage while offering the ability to tune surface chemical properties.[4−9] These architectures minimize precious metal usage and their catalytic properties can be modified, in principle, by altering the size of the active ensembles and their environment.

Fundamental studies have developed extensive structure−function relationships for bimetallic catalysts. Several factors can alter the chemical properties of bimetallic surfaces compared with the pure metals, including so-called strain, ligand, and ensemble effects. As model analogs of core−shell structures, researchers have studied single-crystal bimetallic surfaces consisting of a monolayer of one type of metal covering a bulk metal of another type (e.g., Pt/Ni(111)), and shown that the surface chemical properties can be altered through lattice strain introduced into the monolayer by the substrate as well as by the nature of chemical bonding between the monolayer and substrate.[4,5,9] Computations using density functional theory (DFT) have successfully explained these strain and ligand effects in the context of the d-band center model, showing that adsorbate binding strengths correlate with the energy of the d-band center of the metallic surface and that the d-band center shifts in response to changes in the strain

Received: April 20, 2025
Revised: May 29, 2025
Accepted: June 2, 2025
Published: June 12, 2025

https://doi.org/10.1021/acscatal.5c02708

and chemical bonding with the substrate.[4,5,10] For dilute-alloy surfaces, isolated atoms and small ensembles of the active metal can exhibit atomic-like (i.e., nonmetallic) electronic states[11] and limit reactions that would typically occur on active metal ensembles.[1] Such characteristics often give rise to distinct chemical behavior compared with the bulk metal[1] that has promoted extensive research into miscible metal alloys and intermetallic metal compounds.[12,13]

Mixed metal oxides share many potential benefits to metal alloys, have been shown as active catalysts for a variety of chemical transformations, and continue to garner attention as promising materials for new catalytic applications. However, systematic investigations aimed at identifying how strain, ligand, and ensemble effects influence surface chemical properties are sparse for mixed metal oxides compared with bimetallic alloys, in part due to challenges in synthesizing well-defined mixed metal oxide surfaces. Fundamental studies have revealed that metal-oxide clusters deposited on a second metal-oxide can adopt unusual nanoscopic structures, and that surface sites at the boundary between oxide clusters and the host oxide can promote chemical reactions that are not as efficiently brought about on the pure oxides.[14] Experimental work also reveals that ultrathin metal oxide films grown on single-crystal metal surfaces can exhibit distinct chemical properties compared with the bulk metal oxide due to interactions with the metal substrate.[15−17] Computational investigations predict that cation doping can significantly alter the adsorption and reaction properties of metal oxide surfaces. For example, DFT calculations predict that Pt atoms substituted into surface sites of rutile (110) oxides, such as TiO_2, can exhibit localized electronic states that promote facile CH_4 activation,[18,19] while other work predicts that cation doping into $CeO_2(111)$ can introduce states in the band gap that alter the surface reducibility and thus chemical reactivity.[20,21] Oxide reducibility can also be influenced by charge transfer in oxide-supported oxide systems, such as WO_x or MO_x on TiO_2.[22−24] Unfortunately, many of these computational predictions have not been tested experimentally due to difficulties in synthesizing doped or mixed metal oxides in forms suitable for surface science investigations.

The IrO_2−RuO_2 system provides an ideal platform for investigating fundamental aspects of chemisorption on mixed metal oxides. Both IrO_2 and RuO_2 crystallize in the rutile structure and the (110) facet is the thermodynamically preferred surface for each oxide.[25,26] This (110) facet exposes coordinatively unsaturated metal atoms (M_{cus}) that act as binding sites for both IrO_2 and RuO_2. Close lattice matching promotes the growth of low-strain heteroepitaxial IrO_2/$RuO_2(110)$ thin films, and bulk solutions of IrO_2−RuO_2 can be synthesized over the entire range of cation compositions.[27−29] Recent work shows that heteroepitaxial IrO_2/$RuO_2(110)$ thin films can be synthesized in ultrahigh vacuum (UHV) using vapor deposition methods, and that the initial growth occurs in a nearly layer-by-layer manner such that a single layer ("1L") of $IrO_2(110)$ develops in high coverage on $RuO_2(110)$ before thickening into a multiple layer ("nL") film.[27] In the present study, we utilized this characteristic of the oxide growth to investigate O and N_2 chemisorption on single- and multilayer heteroepitaxial thin films of $IrO_2(110)$ and $RuO_2(110)$ under well-defined UHV conditions.

Our motivation for investigating IrO_2 and RuO_2 in the present study also comes from their use as catalysts for promoting the electrochemical oxygen evolution reaction (OER), alkane oxidation, and the potential benefits that may be realized from employing mixed IrO_2−RuO_2 structures for these applications.[30−39] Pure RuO_2 is well-known to be highly active for the anodic OER but lacks the stability needed for commercial use due to facile dissolution of Ru under acidic conditions. In contrast, IrO_2 exhibits superior stability but is significantly less active than RuO_2. The rationale for using mixed IrO_2−RuO_2 as OER catalysts is thus to combine the high activity of RuO_2 with the high stability of IrO_2 into a single material. Indeed, both core−shell structures and solid solutions of IrO_2−RuO_2 have shown promise as OER catalysts,[33,40,41] but the origin of the improved catalytic performance of these materials is not fully understood. The $IrO_2(110)$ surface also exhibits unusually high reactivity for the activation of light alkanes, and its combination with $RuO_2(110)$ or other oxides may provide opportunities for developing IrO_2-based catalysts for converting light alkanes to value-added products.[42−47]

Additionally, we desire not only to explore how different cation compositions affect adsorption energies, but also to understand the electronic interactions that underlie these effects. While approaches such as the d-band center model are often employed to explain these *element effects* on metallic surfaces, less work has been done on understanding these effects in metal oxides. To this end, we have developed a novel framework for analyzing element effects on metal oxides that is based on computational alchemy[48] and entanglement decomposition. This approach allows us to explain the changes in adsorption energies caused by the substitution of one metal cation with another in terms of the electron transfer occurring during chemisorption.

In the present study, we used temperature-programmed desorption (TPD) to determine the adsorption energies of O and N_2 on synthesized rutile IrO_2−$RuO_2(110)$ heterostructures, finding that O and N_2 bind more weakly on 1L-IrO_2/RuO_2 than pure IrO_2, but more strongly on 1L-RuO_2/IrO_2 than RuO_2. DFT calculations show that these differences are caused almost entirely by the subsurface metal−oxygen ligands directly beneath the M_{cus} binding site, predicting that adsorbate binding on these oxide surfaces is determined primarily by the cations at the surface site and two subsurface sites, regardless of the cations in other lattice sites. From analysis of the chemical bonding, we show that localization of the σ system involved in adsorbate binding on these rutile oxides causes charge accumulation on the O atom beneath the cation binding site, and that replacing Ru with Ir in the neighboring subsurface sites stabilizes this charge and thereby strengthens N_2 and O binding. Our findings provide new insights for understanding the bonding of adsorbates on rutile oxide surfaces, and reveal strong ligand effects that may be utilized for tuning the catalytic properties of mixed metal-oxides.

■ METHODS

$IrO_2(110)$/$RuO_2(110)$ and $RuO_2(110)$/$IrO_2(110)$ Film Growth. We investigated the binding strengths of N_2 and O chemisorbed on two types of heteroepitaxial thin films as a function of the coverage of the deposited oxide, namely, $IrO_2(110)$ on $RuO_2(110)$ and $RuO_2(110)$ on $IrO_2(110)$. Experimental details are provided in the Supporting Information (SI, Section S1). N_2 and O were selected for these experiments to probe the binding properties of the oxide films and avoid oxide reduction during TPD. Initially,

$IrO_2(110)$ was grown in steps on $RuO_2(110)$ using Ir vapor deposition in UHV, following a previously reported approach, where the $RuO_2(110)$ substrate was an ∼ 13-layer film generated by oxidizing Ru(0001) with an O atom beam.[27,28] Close lattice matching facilitates the epitaxial growth of $IrO_2(110)$ on $RuO_2(110)$ ($\Delta a/a$ = +0.3%, $\Delta c/c$ = +1.5%), and mixing of the Ir and Ru cations is avoided by maintaining the substrate temperature below 700 K.[49] For each IrO_2 coverage, we collected N_2 TPD spectra after adsorbing N_2 to saturation at 94 K, followed by O_2 TPD after dissociatively adsorbing O_2 to saturation at 300 K. The TPD measurements were discontinued at a temperature of 650 K to avoid reduction of the oxides. After forming a thick $IrO_2(110)$ film (>∼5 layers), we used TPD to investigate the binding of N_2 and O adsorbed on thin films of $RuO_2(110)$ grown in steps on this thick $IrO_2(110)$ film by Ru vapor deposition in UHV (SI, Section S1). The N_2 and O_2 TPD spectra could be reproduced several times for each IrO_2 and RuO_2 coverage studied, demonstrating that all of the oxide structures remained stable during the experiments.

The quantity ("coverage") of $IrO_2(110)$ generated on $RuO_2(110)$ is specified in terms of "layers", where 1-layer is equivalent to the separation of 0.318 nm between the cation planes of rutile IrO_2 measured along the [110] direction. The $IrO_2(110)$ coverages were estimated from the total Ir fluence to surface, after calibrating the Ir flux from measurements of the attenuation of Ru peaks in Auger electron spectroscopy (SI, Section S2).[28,49,50] The coverage of RuO_2 grown on $IrO_2(110)$ is defined similarly, and was also estimated by calibrating the Ru incident flux to the surface. The uncertainties in the IrO_2 and RuO_2 coverages generated by vapor deposition are estimated as 6% and 10%, respectively, based on the flux calibrations (Section S2). In general, the number of layers should be regarded as an approximation of the quantity of IrO_2 or RuO_2 rather than describing the morphology of the oxide film. Importantly, previous measurements using scanning tunneling microscopy (STM) demonstrate that an $IrO_2(110)$ film grows initially in a nearly layer-by-layer mode on $RuO_2(110)$,[27,51] such that $IrO_2(110)$ domains of monolayer thickness ("single layer" = 1L) form in coverages up to at least 0.6 layers, before thickening and transforming to a multilayer $IrO_2(110)$ film ("multi-layer" = nL). STM measurements also show that the $RuO_2(110)$ substrate becomes completely covered after generating an approximately 2-layer thick $IrO_2(110)$ film.[21]

Figure 1 shows a ball and stick model of the rutile $MO_2(110)$ surface formed by IrO_2 and RuO_2. The $MO_2(110)$ surface has a rectangular unit cell and is composed of alternating rows of coordinatively unsaturated metal atoms (M_{cus}) and bridging O atoms (O_{br}) along the [001] direction. The M_{cus} and O_{br} atoms each have single coordination vacancies due to a decrease in bond coordination relative to bulk MO_2; the M_{cus} atoms have 5-fold coordination, whereas bulk M atoms have 6-fold coordination, and O_{br} atoms have 2-fold coordination, whereas bulk O atoms have 3-fold coordination. The coordination vacancy on the M_{cus} atom is directed along the surface normal and lies in the axial position of the local octahedral geometry. Because the M_{cus} atoms are the active adsorption sites of $IrO_2(110)$ and $RuO_2(110)$, an adsorbate coverage of 1 ML ("monolayer") is defined as the density of M_{cus} atoms on the (110) surfaces. Prior studies show that molecular N_2 adsorbs in an upright configuration on top of the M_{cus} atoms of these oxides,[28,52,53] while O_2 undergoes facile dissociative chemisorption on the M_{cus} rows at 300 K and produces O atoms that adsorb directly on-top (O_t) of M_{cus} atoms (Figure 1).[25,26,54−56]

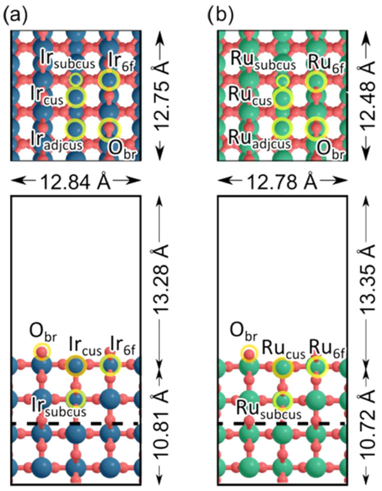

Figure 1. Top and side view of (a) $IrO_2(110)$ and (b) $RuO_2(110)$ with cus metal atoms (M_{cus}) labeled, as well as their neighbors: one at an adjacent cus position (M_{adjcus}), one in a 6-fold coordination site, M_{6f}, beneath bridging O atoms, O_{br}, and one in the subsurface (M_{subcus}) beneath the M_{cus} site. Under the dashed lines represent the bottom two layers of the $MO_2(110)$ surfaces, which were fixed at their bulk position during DFT calculations. Green atoms represent Ru, dark blue atoms represent Ir, and red atoms represent O.

RESULTS

N_2 and O_2 Desorption from Multilayer $RuO_2(110)$ and $IrO_2(110)$.

Adsorbed N_2 binds more strongly on nL-$IrO_2(110)$ compared with nL-$RuO_2(110)$. After generating a saturated N_2 layer at 94 K, TPD experiments (Figure 2a) show that molecularly adsorbed N_2 desorbs from nL-$RuO_2(110)$ in two distinct peaks at 130 and 175 K, and that N_2 desorption is complete by about 200 K. The higher temperature peak is attributed to N_2 that desorbs from low-coverage configurations in which the N_2 has few nearest neighbors, while the lower temperature peak arises from N_2 that is destabilized by neighboring N_2 molecules in the layer. For nL-$IrO_2(110)$, the N_2 TPD trace exhibits a maximum at 275 K and a pronounced shoulder at 245 K. The less intense desorption features near 115 and 180 K have been attributed previously to N_2 desorbing from kinetically trapped states that populate during adsorption at low temperature (94 K); these features originate from IrO_2 since low energy ion scattering spectroscopy shows that nL-IrO_2 coverages above at least 3 layers completely cover the underlying $RuO_2(110)$ substrate.[28] A prior study also shows that the main TPD peak at 275 K originates from N_2 desorbing from low-coverage configurations on nL-$IrO_2(110)$, while the peak at 245 K arises from N_2 desorption from less stable, high-coverage configurations.[28] Thus, in the low coverage limit, the TPD peak is 100 K higher for the desorption of molecularly adsorbed N_2 from nL-$IrO_2(110)$ compared with nL-$RuO_2(110)$. From analysis of the TPD peak temperatures, we estimate that the N_2 adsorption energy at low coverage is -59 vs -96 kJ mol^{-1} for N_2 adsorbed on $RuO_2(110)$ vs $IrO_2(110)$ (SI, Section S3), in good agreement with prior work.[28,52]

Chemisorbed O_t-atoms also bind more strongly on nL-$IrO_2(110)$ compared with nL-$RuO_2(110)$. On nL-$RuO_2(110)$,

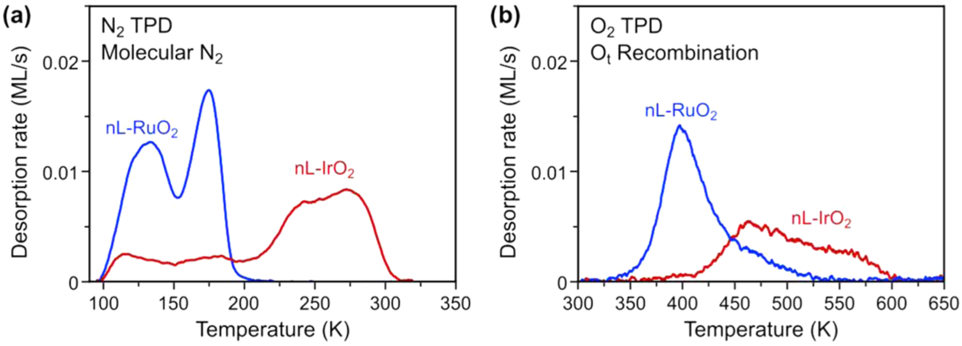

Figure 2. TPD traces of (a) N_2 and (b) O_2 obtained from nL-RuO_2(110) (blue) and nL-IrO_2(110) (red) after saturating each surface with N_2 at 94 K or O_t atoms at 300 K. N_2 adsorbs and desorbs nondissociatively on M_{cus} atoms whereas O_2 desorption results from the recombination of O_t atoms on M_{cus} atoms. The thicknesses of the nL-RuO_2(110) and nL-IrO_2(110) films were about 13 and 5 layers, respectively.

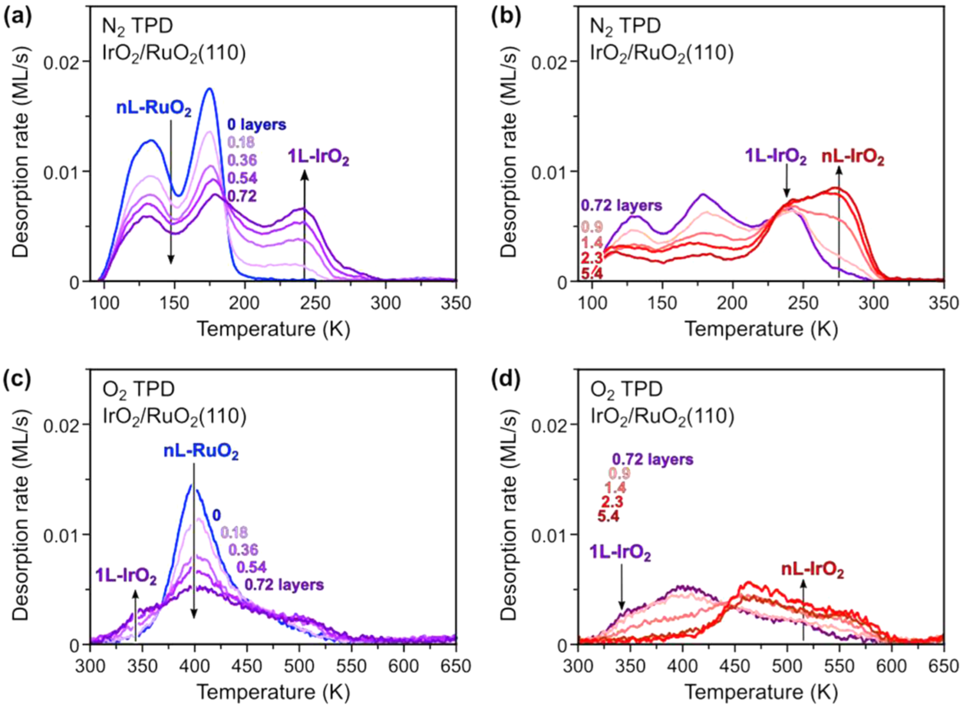

Figure 3. TPD spectra of (a−b) N_2 and (c−d) O_2 obtained as a function of the IrO_2(110) coverage (0 to 5.4 layers) grown on a nL-RuO_2(110) surface. Prior to each TPD measurement, N_2 was adsorbed to saturation at 94 K and subsequently O_2 was dissociatively adsorbed to generate a saturated O_t layer. Data are shown for IrO_2(110) coverages of (a, c) 0 to 0.72 layers and (b, d) 0.72 to 5.4 layers, where 0.72 layers (purple) coincides approximately with the maximum coverage of 1L-IrO_2(110) based on TPD.

the recombinative desorption of O_t atoms generates a TPD peak at 400 K and a broad trailing edge that extends to about 525 K. Chemisorbed oxygen desorbs at comparatively higher temperatures from nL-IrO_2(110), with the O_2 TPD trace rising to a maximum at 463 K and thereafter decreasing to the baseline once the temperature reaches 600 K. The considerable widths of the O_2 TPD features is a topic for future study, and have been previously attributed to repulsive interactions among coadsorbed O_t atoms, site heterogeneity and kinetic effects.[25,54−61] From analysis of the TPD peak temperatures, we estimate that the barriers for recombinative desorption of O_t atoms are 146 and 171 kJ mol^{-1} on multilayer RuO_2(110) and IrO_2(110), respectively, for comparable O_t coverages of about 0.5 ML (SI, Section S3).

Adsorbate Destabilization on Single-Layer IrO_2(110) on RuO_2(110). To probe the binding characteristics of single-layer IrO_2(110), TPD spectra for adsorbed N_2 and O_t were acquired as a function of the IrO_2(110) coverage generated on a thick RuO_2(110) film. The evolution of the N_2 and O_2 TPD spectra with the IrO_2(110) coverage (Figure 3) show isosbestic points and are consistent with the nearly exclusive growth of 1L-IrO_2(110) domains up to high IrO_2(110) coverage (~0.7 layers), with film thickening occurring thereafter, in good agreement with previous STM measurements.[27] As seen in Figure 3a, the N_2 TPD peaks from nL-RuO_2(110) (130, 175 K) diminish sharply as the IrO_2(110) film thickness is increased stepwise to 0.72 layers, demonstrating that the IrO_2(110) film covers an increasing fraction of the RuO_2(110) substrate during the early stages of IrO_2 growth. The shapes and positions of these nL-RuO_2(110) peaks remain largely unchanged with IrO_2(110) film thickness, suggesting that the single-layer IrO_2(110) film forms large islands on the surface and preserves RuO_2 domains large enough for N_2 to influence one another through coadsorbate interactions, which

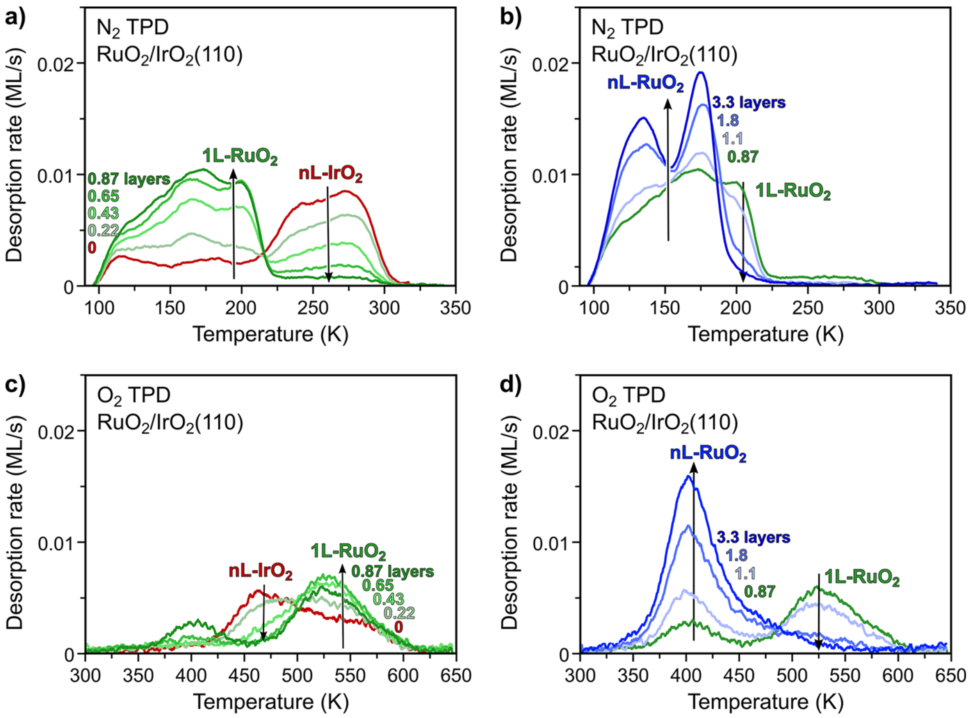

Figure 4. TPD spectra of (a−b) N_2 and (c−d) O_2 obtained as a function of the $RuO_2(110)$ coverage (0 to 3.3 layers) grown on a nL-$IrO_2(110)$ surface. Prior to each TPD measurement, N_2 was adsorbed to saturation at 94 K and subsequently O_2 was dissociatively adsorbed to generate a saturated O_t layer. Data are shown for $RuO_2(110)$ coverages of (a, c) 0 to 0.87 layers and (b, d) 0.87 to 3.3 layers. The TPD data suggests that the maximum coverage of 1L-$RuO_2(110)$, green, is obtained at a $RuO_2(110)$ coverage between 0.65 and 0.87 layers.

is consistent with prior STM observations.[27] A N_2 TPD peak at about 240 K intensifies while the peaks from N_2 on nL-$RuO_2(110)$ diminish, but the peak at 275 K (expected for N_2 on nL-$IrO_2(110)$) remains small (Figure 3a). This peak at 240 K represents N_2 desorption from 1L-$IrO_2(110)$ domains, and thus increases as the surface goes from 0 to 0.72 $IrO_2(110)$ layers. As the $IrO_2(110)$ thickness is increased above 0.72 layers (Figure 3b), the N_2 TPD peaks below 200 K diminish more gradually, and the TPD intensity near 240 K remains roughly constant. The peak at 275 K begins to intensify above ∼0.7 layers, with its intensity increasing more sharply as the $IrO_2(110)$ coverage is increased from 0.9 to 2.3 layers. The N_2 TPD spectrum obtained for an $IrO_2(110)$ coverage of 2.3 layers closely resembles those obtained for thicker $IrO_2(110)$ films (Figures 2a and 3b),[28] suggesting that the surface chemical properties of $IrO_2(110)$ films on $RuO_2(110)$ become similar to those of bulk $IrO_2(110)$ at a film thickness of only about 2 layers.

The N_2 TPD spectra demonstrate that N_2 binds more weakly on 1L-$IrO_2(110)$ compared with nL-$IrO_2(110)$. First, the low intensity of the TPD peak at 275 K shows that multilayer $IrO_2(110)$ forms in minimal quantities for IrO_2 coverages below at least 0.7 layers. As such, for low IrO_2 coverages (<∼ 0.7 layers), the N_2 TPD peak at 240 K is attributed to the desorption of N_2 adsorbed in low coverages on 1L-$IrO_2(110)$ domains. Similar to nL-$IrO_2(110)$, we suggest that N_2 at high coverage on 1L-$IrO_2(110)$ is destabilized by intermolecular interactions and desorbs in the broad TPD feature below 240 K (Figure 3a). The N_2 TPD intensity near 240 K remains constant rather than decreasing as the film thickness increases beyond 0.7 layers and 1L-$IrO_2(110)$ domains are replaced by nL-$IrO_2(110)$ (Figure 3b). This behavior is consistent with the peak at 240 K arising from both low coverages of N_2 on 1L-$IrO_2(110)$ and high coverages of N_2 on nL-$IrO_2(110)$. From analysis of the TPD peak temperatures (240 vs 275 K), we conclude that, in the limit of low N_2 coverage, the adsorption energy for N_2 is 13 kJ mol^{-1} less exothermic (weaker binding) from 1L-$IrO_2(110)$ on $RuO_2(110)$ compared with nL-$IrO_2(110)$.

O_t atoms, like N_2, are destabilized on 1L-$IrO_2(110)$ relative to nL-$IrO_2(110)$ and are more destabilized than N_2. As the IrO_2 coverage is initially increased, the main O_2 TPD peak at 400 K arising from O_t desorption from nL-$RuO_2(110)$ diminishes and a new O_2 peak at 340 K concurrently intensifies, reaching a maximum at an IrO_2 coverage of ∼ 0.7 layers (Figure 3c). A small O_2 TPD feature centered at about 510 K also develops, and is likely associated with O_t atoms desorbing from nL-$IrO_2(110)$ domains. The O_2 TPD peak at 340 K diminishes sharply as the IrO_2 coverage increases from 0.9 to 2.3 layers, while the TPD intensity above 450 K increases. Similar to the behavior seen for N_2, the O_2 TPD trace obtained from a 2.3-layer $IrO_2(110)$ film on $RuO_2(110)$ closely resembles that obtained from thicker, $IrO_2(110)$ films, further supporting the idea that $IrO_2(110)$ films adopt bulk-like surface chemical properties after thickening to only about 2 layers.

We attribute the O_2 TPD peak at 340 K to O_t atoms desorbing recombinatively from 1L-$IrO_2(110)$ domains because the evolution of this TPD feature with increasing IrO_2 coverage mirrors the formation and consumption of 1L-$IrO_2(110)$ domains. The O_2 TPD data thus indicates that O_t atoms bind more weakly on 1L-$IrO_2(110)$ compared with nL-$IrO_2(110)$, similar to N_2. From the TPD peak temperatures (340 vs 463 K), we conclude that the barrier for the recombinative desorption of O_t atoms to form O_2 is 47 kJ mol^{-1} lower from 1L-$IrO_2/RuO_2(110)$ compared with nL-

Table 1. Adsorption Energies of N_2 and O_t Estimated from TPD Experiments Performed with Single and Multilayer $IrO_2(110)$ and $RuO_2(110)$ Thin Films of IrO_2/RuO_2 Heterostructures[a]

comparing 1st layer				comparing subsurface			
		N_2	O_t			N_2	O_t
nL-IrO_2	*Ir above Ir*	−96	−86	nL-IrO_2	*Ir above Ir*	−96	−86
1L-RuO_2/IrO_2	*Ru above Ir*	−68	−100	1L-IrO_2/RuO_2	*Ir above Ru*	−83	−62
ΔE $(IrO_2-RuO_2)/IrO_2$		−28	+14	ΔE $IrO_2/(IrO_2-RuO_2)$		−13	−24
1L-IrO_2/RuO_2	*Ir above Ru*	−83	−62	1L-RuO_2/IrO_2	*Ru above Ir*	−68	−100
nL-RuO_2	*Ru above Ru*	−59	−73	nL-RuO_2	*Ru above Ru*	−59	−73
ΔE $(IrO_2-RuO_2)/RuO_2$		−24	+11	ΔE $RuO_2/(IrO_2-RuO_2)$		−9	−27
average shift:				**average shift:**			
ΔE (IrO_2-RuO_2) 1st layer		**−26**	**+13**	**ΔE (IrO_2-RuO_2) subsurface**		**−11**	**−25**

[a]Energies are given in kJ mol^{-1}, and the O_t adsorption energy is shown on a per-atom basis (rather than per-molecule).

$IrO_2(110)$, corresponding to a decrease from 171 to 124 kJ mol^{-1} on nL vs 1L-$IrO_2(110)$. From those O_2 desorption energies, the adsorption energies (on a per-atom basis) shift from −86 to −62 kJ mol^{-1}, suggesting weaker binding by 24 kJ mol^{-1}, demonstrating a significant destabilization of adsorbed O_t-atoms when the $IrO_2(110)$ thickness on $RuO_2(110)$ is only a single layer.

Among nL-RuO_2, 1L-IrO_2/RuO_2, and nL-IrO_2, we see that N_2 desorption peaks (T_p) trend as $175 < 240 < 275$ K, suggesting that N_2 binds strongest to Ir_{cus} atoms, and that thin IrO_2 films on a RuO_2 substrate bind N_2 weaker than thick IrO_2. For the recombinative desorption of O_t, a different trend emerges, with 1L-IrO_2/RuO_2 (T_p = 340 K) having weaker binding than nL-RuO_2 (T_p = 400 K), followed by nL-IrO_2 (T_p = 463 K).

Adsorbate Stabilization on Single-Layer $RuO_2(110)$ on $IrO_2(110)$. DFT calculations (described below) led us to investigate N_2 and O_t binding on 1L-$RuO_2(110)$ films grown on nL-$IrO_2(110)$. A $RuO_2(110)$ film was grown in steps on a thick, nL-$IrO_2(110)$ film (5.4 layers), which itself was grown on nL-$RuO_2(110)$, and TPD spectra (Figure 4) were acquired from adsorbed N_2 and O_t atoms as a function of the RuO_2 coverage.

TPD experiments of adsorbed N_2 show isosbestic points (as in Figure 3) and provide evidence that the growth of $RuO_2(110)$ on nL-$IrO_2(110)$ produces near-monolayer coverages of 1L-$RuO_2(110)$ before nL-$RuO_2(110)$ forms. N_2 binds more strongly on 1L-RuO_2/IrO_2 compared with nL-RuO_2 (Figure 4a). As the RuO_2 coverage is increased to about 0.9 layers, the N_2 TPD features (>225 K) arising from N_2 on nL-$IrO_2(110)$ diminish into the baseline, while TPD features below 225 K concurrently intensify (Figure 4a). Among these TPD features is a distinct maximum at 200 K that is not observed in N_2 TPD experiments performed with nL-$RuO_2(110)$. The fact that the N_2 TPD features arising from nL-$IrO_2(110)$ diminish into the baseline demonstrates that RuO_2 completely covers the $IrO_2(110)$ substrate as the RuO_2 coverage approaches 1 layer; this behavior is similar to that observed for IrO_2 growth on $RuO_2(110)$ and thus consistent with the growth of high coverages of 1L-$RuO_2(110)$ on the nL-$IrO_2(110)$ film.

As the RuO_2 coverage is increased from about 0.9 to 1.8 layers, the intensity of the N_2 TPD peak at 200 K decreases sharply, while peaks at 130 and 175 K intensify (Figure 4b). The N_2 TPD spectrum obtained from a 1.8-layer $RuO_2(110)$ film resembles those obtained from thicker $RuO_2(110)$ films, suggesting that a film thickness of 2 layers is sufficient for the adsorbate binding properties of $RuO_2(110)$ films on $IrO_2(110)$ to exhibit similar behavior as thicker, bulk-like $RuO_2(110)$ films. Analogous to our results for IrO_2 growth on $RuO_2(110)$, the N_2 TPD peak at 200 K is attributed to molecularly adsorbed N_2 desorbing at low coverages from 1L-$RuO_2(110)$, based on the fact that the evolution of this TPD peak with increasing RuO_2 coverage tracks that for the formation and consumption of 1L-$RuO_2(110)$. For RuO_2 coverages below ∼ 0.9 layers, a large portion of the N_2 TPD intensity below 200 K is attributed to the desorption of N_2 in high-coverages on 1L-$RuO_2(110)$ domains. Based on the TPD peak temperatures (175, 200 K), we estimate that the adsorption energy is 9 kJ mol^{-1} more exothermic for N_2 adsorbed in low coverages on 1L-$RuO_2(110)$ compared with nL-$RuO_2(110)$.

TPD shows that O_t atoms are significantly stabilized on 1L-$RuO_2(110)$ compared with nL-$RuO_2(110)$. As the RuO_2 coverage is increased to 0.65 layers, the O_2 TPD peak at 463 K from O_t desorbing from nL-$IrO_2(110)$ diminishes and a new TPD peak at 530 K intensifies (Figure 4c). The O_2 TPD peak at 400 K from O_t on nL-$RuO_2(110)$ initially remains small and first emerges when the RuO_2 coverage is increased to 0.87 layers, intensifying sharply thereafter as the RuO_2 coverage is increased to 3.3 layers. The development of the O_2 TPD peak at 400 K is accompanied by a decrease in the intensity of the peak at 530 K, particularly as the RuO_2 coverage is increased from about 1 to 1.8 layers (Figure 4d). This behavior is attributed to the replacement of 1L-RuO_2 domains by nL-RuO_2 as the RuO_2 coverage is increased above about 0.65 layers. The O_2 TPD peak at 530 K is attributed to the recombinative desorption of O_t atoms from 1L-RuO_2 based on its evolution with the RuO_2 coverage. From the TPD peak temperatures, we estimate that the adsorption energy is 27 kJ mol^{-1} more exothermic for O_t atoms on 1L-RuO_2 compared with nL-RuO_2, and about 13 kJ mol^{-1} more exothermic on 1L-RuO_2 relative to nL-IrO_2.

A comparison of the adsorption energy differences estimated from TPD reveals key influences of the first and second layers of the IrO_2/RuO_2 heterostructures. Comparing these adsorption energies (Table 1) shows that replacing Ru with Ir in the first layer (including the binding site) weakens the binding of O_t (by about 12 kJ mol^{-1}), and strengthens the binding of N_2 (by about 26 kJ mol^{-1}). These shifts are similar whether you compare structures with RuO_2 or IrO_2 in the second layer (substrate); the shifts brought about by changes in the first layer are independent of the identity of the second layer. Below we show that N_2 and O_t have different preferences in their binding metals because of electronic localization effects that are distinct for these rutile oxides. When considering a replacement of Ru with Ir in the second layer (beneath the

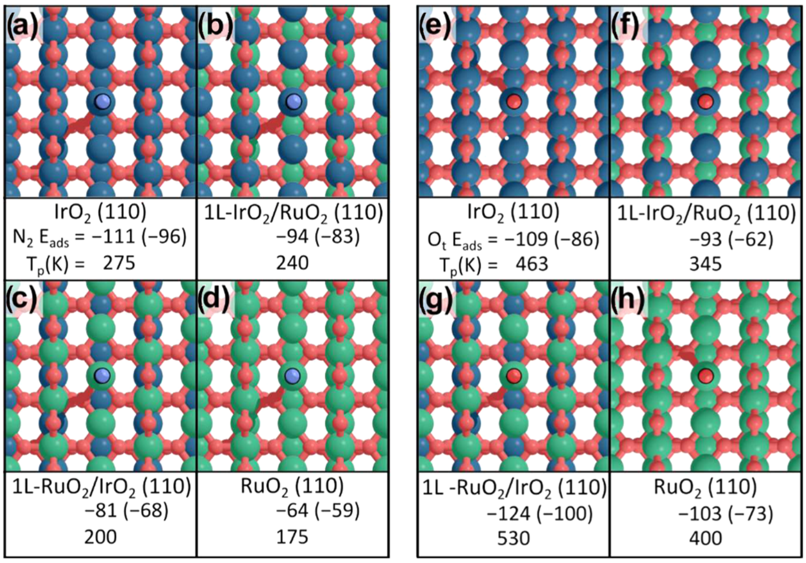

Figure 5. Structures, adsorption energies (E_{ads}), and TPD peak temperatures (T_p, in K) of N_2 and O_t on $MO_2(110)$ surfaces. TPD-estimated binding energies (Table 1) are shown in parentheses for reference. N_2 on (a) IrO_2, (b) 1L-IrO_2/RuO_2, (c) 1L-RuO_2/IrO_2, and (d) RuO_2 surfaces, and O_t on (e) IrO_2, (f) 1L-IrO_2/RuO_2, (g) 1L-RuO_2/IrO_2, and (h) RuO_2 surfaces. Green atoms represent Ru, dark blue atoms represent Ir, light blue atoms represent N, and red atoms represent O.

binding site), we see that the binding energies of both O_t and N_2 are strengthened, by about 11 and 25 kJ mol^{-1}, respectively, when either IrO_2 or RuO_2 is in the first layer (Table 1).

DFT Calculations of N_2 and O_t Binding on the Single, Multilayer, and Atomically Mixed Oxides. Spin-polarized DFT calculations (computational details in Section S4 of SI) were performed using the PBE exchange-correlation functional to corroborate these observed trends by calculating binding energies of N_2 and O_t on M_{cus} sites of (110) surfaces of IrO_2, 1L-IrO_2/RuO_2, 1L-RuO_2/IrO_2, and RuO_2. N_2 binding strength trends as IrO_2 > 1L-IrO_2/RuO_2 > 1L-RuO_2/IrO_2 > RuO_2, with adsorption energies of $-111 < -94 < -81 < -62$ kJ mol^{-1}, respectively (Figure 5a−d). These results are consistent with the N_2 TPD results (Figures 3−4). O_t binding strength trends as 1L-RuO_2/IrO_2 > IrO_2 > RuO_2 > 1L-IrO_2/RuO_2, with adsorption energies of $-124 < -109 < -103 < -93$ kJ mol^{-1}, respectively (Figure 5e−h). As with N_2, this data is consistent with TPD measurements (Figures 3−4). To test for effects of strain we compare adsorption energy calculations for N_2 and O_t for IrO_2 using the unit cell parameters of RuO_2 (and vice versa, running pure RuO_2 with the unit cell parameters of IrO_2). Strain affected N_2 and O_t adsorption energies by less than 5 kJ mol^{-1} (Table S3 of the SI) far less than the shifts caused by changes in the subsurface shown in Figure 5.

Comparing adsorption energies for structures with IrO_2 and RuO_2 in the first layer (with the same subsurface structure) shows that for N_2, binding is stronger with IrO_2 in the first layer, by 30 kJ mol^{-1}, whether the subsurface is IrO_2 (i.e., comparing IrO_2 and 1L-RuO_2/IrO_2) or RuO_2 (i.e., comparing 1L-IrO_2/RuO_2 and RuO_2). This preference for IrO_2 in the first layer, by 30 kJ mol^{-1}, is very close to the shift in TPD-estimated adsorption energies (26 kJ mol^{-1}, Table 1). For O_t atoms, in contrast, binding is stronger with RuO_2 in the first layer, with DFT-predicted binding energies shifting by an average of 13 kJ mol^{-1}, identical to TPD-estimated shifts (Table 1). In examining the effects of cations in the second layer, DFT predicts that the binding of both N_2 and O_t is stronger with IrO_2 in the second layer. For N_2, the adsorption energy gets 17 kJ mol^{-1} more exothermic, regardless of whether the first layer is IrO_2 or RuO_2, and this is similar to the TPD-predicted shift of 11 kJ mol^{-1} (Table 1). For O_t, the adsorption energy gets 18 kJ mol^{-1} more exothermic (on average), again similar to the shift estimated from TPD (25 kJ mol^{-1}).

Comparing DFT-calculated adsorption energies and those estimated from TPD suggests that DFT overestimates N_2 binding strength by 5−15 kJ mol^{-1}, with the gap being largest on strong-binding IrO_2 (15 kJ mol^{-1}) and smallest on weak-binding RuO_2 (5 kJ mol^{-1}). For O_t, DFT also overpredicts binding strength, and by a larger margin, with adsorption energies being 23−31 kJ mol^{-1} too exothermic compared to the TPD-estimated values. While the errors do not correlate with binding strength, as they do for N_2, they seem to be smaller for structures with IrO_2 in the subsurface (IrO_2 and 1L-RuO_2/IrO_2, errors of ∼24 kJ mol^{-1}) than for structures with RuO_2 in the subsurface (RuO_2 and 1L-IrO_2/RuO_2, errors of ∼30 kJ mol^{-1}). Adsorption energies estimated from TPD spectra can vary based on assumptions made in the analysis, such as the choice of pre-exponential factors, how the effects of coverage are considered, and experimental factors such as the temperature ramp rate. In Table S2, we compare DFT-predicted adsorption energies with and without spin-polarization from PBE, RPBE, and BEEF exchange-correlation functionals. All three functionals overpredict the binding strength of O_t, with RPBE coming closest to the TPD-estimated values; for example, RPBE predicts an adsorption energy for O_t on IrO_2 (−94 kJ mol^{-1}), compared to PBE (−109 kJ mol^{-1}), BEEF (−107 kJ mol^{-1}), and TPD (−86 kJ mol^{-1}). For N_2, PBE overpredicts the binding strength (−111 kJ mol^{-1} on IrO_2) compared to TPD (−96 kJ mol^{-1}), while RPBE underpredicts it (−83 kJ mol^{-1}), and BEEF falls in between (−103 kJ mol^{-1}), closest to the TPD estimates. Critically, the trends among materials are nearly identical regardless of which functional is used.

DFT was also used to corroborate that two-layer films behave like thick films, as suggested by the TPD experiments.

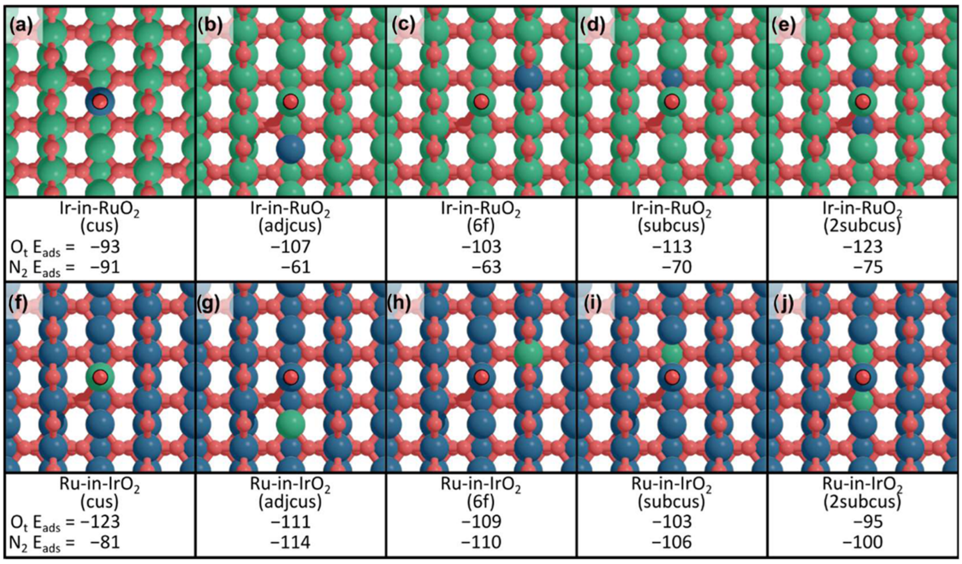

Figure 6. Structures (pictured for O_t) and adsorption energies (E_{ads}) of N_2 and O_t on (110) surfaces of Ir doped into $RuO_2(110)$ at the (a) cus, (b) adjcus, (c) 6f, (d) subcus, and (e) 2 subcus positions with analogous structures shown in (f–j) for Ru doped into an $IrO_2(110)$ surface. Green atoms represent Ru, dark blue atoms represent Ir, and red atoms represent O.

DFT-calculated adsorption energies varied by <10 kJ mol^{-1} for N_2 and O_t between (110) surfaces of RuO_2 and a two-layer RuO_2/IrO_2 model, and between IrO_2 and a two-layer IrO_2/RuO_2 model (Figure S5 and S4 in SI). These data suggest that two-layer films would behave as thick films, and therefore the TPD features which arise with the coverage of IrO_2/RuO_2 and the coverage of RuO_2/IrO_2 reflect single-layer films that are raft-like and grow conformally over the surface rather than as dispersed MO_x sites or as multilayer MO_x clusters, consistent with prior STM experiments.[27] Thus, bonding at the IrO_2–RuO_2 interface has a highly localized influence on surface adsorption properties as it can strongly affect the binding of adsorbates on single-layer films but has a negligible influence on the adsorption properties of films with only 2-layers of oxide.

Next, we consider atomically mixed IrO_2–RuO_2 structures (in contrast to the layered materials described above) to understand how atomic arrangements present in those layers influence surface binding properties. First, we show the effects of doping a single Ir atom into a $RuO_2(110)$ surface. M_{cus} binding sites have three distinct adjacent cations (Figure 1): two in adjacent cus sites (adjcus), four in 6-fold (6f) surface sites, and two beneath the cus site (subcus). Doping Ir at the M_{cus} binding site results in a surface with nearly identical binding energies to the 1L-IrO_2/RuO_2 surface—stronger binding than RuO_2 for N_2, but weaker binding than RuO_2 for O_t (Figure 6a). Placing the Ir in an M_{adjcus}, M_{6f}, or M_{subcus} sites, causes the Ru_{cus}–O_t bond to strengthen compared to RuO_2, with the strongest shift occurring when Ir is placed in the subcus site (Figure 6b–d). For N_2 adsorption, the placement of Ir in the adjcus or 6f sites has little impact, while placement in the subcus site creates a stronger Ru_{cus}–N_2 bond, as observed with O_t (Figure 6b–d). The increase in binding strength with Ir in the subcus positions is even stronger when both subcus sites are Ir (2subcus, Figure 6e), for which the O_t binding energy is −123 kJ mol^{-1}, very similar to that for 1L-RuO_2/IrO_2 (−125 kJ mol^{-1}), while the N_2 binding energy (2subcus) is −75 kJ mol^{-1}, just shy of the −81 kJ mol^{-1} predicted for 1L-RuO_2/IrO_2. Future experiments are planned to synthesize atomically mixed oxides and investigate their adsorbate binding properties.

These atomically mixed surfaces suggest that the binding properties are most strongly governed by the identity of the metal in the M_{cus} binding site, as well as the identity of the metals directly beneath (subcus). To further demonstrate this, we show the calculated binding energies for O_t and N_2 on ~60 pure and mixed metal oxide surfaces, including the pure and layered structures (Figure 5) as well as atomically mixed structures (Figure 6 with more shown in Figures S4 and S5 in the SI). The results show that Ir_{cus}–N_2 bonds are ~30 kJ mol^{-1} stronger than those for Ru_{cus}, while the opposite is seen for O_t, where Ir_{cus}–O_t bonds are ~20 kJ mol^{-1} weaker than those for Ru_{cus}, as seen from the y-intercepts of Figure 7 (corresponding to adsorption onto sites with no Ir in the subcus positions). Examining the effect of the subsurface, increasing the number of Ir atoms in the two subcus positions (from Ru_2, to IrRu, to

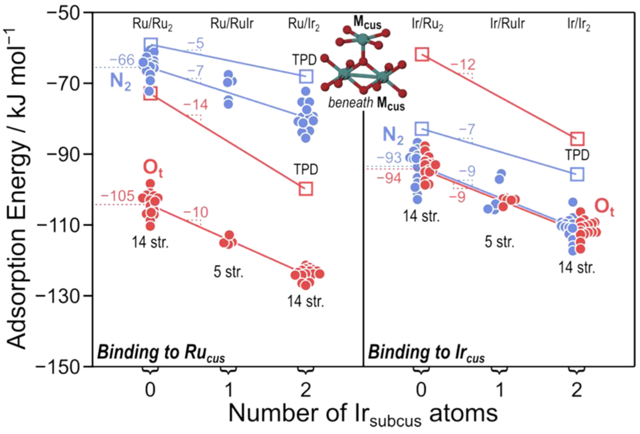

Figure 7. Adsorption energies of N_2 (blue) and O_t (red, referenced to 1/2 O_2 gas) when bound to Ru_{cus} atoms (left) and Ir_{cus} atoms (right) with varying amounts of Ir atoms in the two subcus sites. DFT-calculated values are filled circles, energies estimated from TPD spectra are hollow squares. Figure S4 and S5 in the SI show greater details for the mixed-metal oxide surfaces depicted here.

Ir_2 compositions) strengthens the adsorption of O_t and N_2 to similar extents for each Ir_{subcus} cation (−8 and −10 kJ mol^{-1} $Ir_{subcus}{}^{-1}$ for N_2 and O_t), as seen in the slopes shown in Figure 7. The scatter seen within each set of data reflects the impacts of the identities of other cations (e.g., in adjcus or 6f positions) in the top two layers of the surface. The strong effect of subcus cations may be explained by the geometry of the cus binding site. M_{cus} atoms coordinate with five O atoms in an octahedral geometry with four O atoms in the equatorial plane and one O atom located directly beneath the M_{cus} atom, in the position trans to the N_2 or O_t adsorbate. Each O atom in the surface plane bonds with an adjcus and 6f surface M atoms, while the subsurface O atom bonds to two subcus M atoms. This suggests that these strong effects of the composition of the subcus atoms is related to a trans-ligand effect by influencing the O beneath the cus site, similar to those described in organometallic literature,[62] demonstrated here for an oxide surface.

Origin of the Site and Ligand Effects. A puzzling aspect of the DFT and experimental results is that the effect of cation identity (i.e., the element effect) on O_t chemisorption associated with exchanging Ru and Ir in the two subsurface metal ligands is opposite in sign to the element effect resulting from exchanging Ru and Ir at the binding site. Specifically, Ru_{cus} binds O_t more strongly than Ir_{cus} (site effect), whereas Ru_{subcus} weakens binding of O_t compared to Ir_{subcus} (ligand effect). Thus, the element effect in these oxides is inverted on the ligand with respect to the effect observed in metals for O_t adsorption.

To understand the origin of the inverted element effect on O_t chemisorption associated with the subsurface metal ligands in these oxide surfaces, we start by introducing a framework for understanding element effects in general that is based on the concept of computational alchemy.[48] Computational alchemy treats the atomic number of each atom as a continuous variable, allowing one to gradually transmute one element into another. This allows the element effect associated with atom i in the surface to be expressed as the partial derivative of the binding energy ΔE_{ads} with respect to the atomic number, Z_i, of that atom

$$\frac{\partial \Delta E_{ads}}{\partial Z_i} = \Delta \phi_i + \Delta \varepsilon_F \tag{1}$$

The first term is the change in electrostatic potential at the nucleus of atom i induced by chemisorption, accounting for the increase in nuclear charge, while the second term is the change in Fermi level induced by chemisorption, accounting for the electron that must be added to maintain charge neutrality. The change in Fermi level will vanish in the limit of a semi-infinite surface so it can be neglected in any conceptual understanding of the element effect; however, it is not negligible in practical applications utilizing a periodic slab model. In the framework of pseudopotential methods, the atomic number can be approximately replaced by the net charge of the ionic core (nucleus plus core electrons) of a fixed shape, so that exchanging Ru with Ir corresponds to both an increase in the ionic core charge by one unit with the corresponding increase in the valence as well as a change in the ionic core shape (going from row 4d to 5d).

The computational alchemy framework indicates that the elemental effect for a given metal atom is positive (adsorbate binding strengthens) if the chemisorption process decreases the electrostatic potential at the metal nucleus and is negative if the chemisorption process increases the potential at the metal nucleus. For a metal oxide, the potential at the metal nucleus is mainly determined by the partial charge on the metal atom and somewhat less from the partial charges on the oxygen atoms neighboring it. It can be deduced that a positive element effect will be associated with a metal atom that gains electron density during the chemisorption process, while a negative element effect will be associated with a metal atom that loses electron density during the chemisorption process. This rule applies to any metal atom in the surface, regardless of whether it is in the binding site itself, is a ligand of the binding site, or is further away. This means that the negative element effect associated with the adsorption site during O_t chemisorption arises from a depletion of electron density on the site upon adsorption, which is destabilized by the increase in the positive charge of the ionic core when Ru is exchanged with Ir. Likewise, the positive element effect associated with N_2 chemisorption arises from an accumulation of electron density on the site, which is stabilized by the increase in ionic core charge.

To quantify charge accumulation or depletion on specific atoms, charge is assigned to atomic orbitals using the quasi-atomic orbital (QO) method developed by Qian et al.[63] and implemented by Plaisance and co-workers[64] into VASP. The QO method constructs a tight binding basis set (the quasi-atomic orbitals) from a plane wave DFT calculation that exactly reproduces the occupied bands of the latter. The resulting QOs resemble atomic orbitals that are slightly distorted due to the chemical environment and allow for the use of population analysis techniques like those used in the study of molecular systems in atomic orbital basis set codes. Using this approach allows us to quantify the amount of charge accumulation or depletion induced by the electronic transformations described above.

This behavior is shown clearly in Figure 8, where it can be seen that chemisorption of O_t leads to a depletion of 0.20 e on the adsorption site, while N_2 leads to an accumulation of 0.10 e. Essentially, increasing the positive charge on the ionic core of M_{cus} when exchanging Ru with Ir stabilizes the electron accumulation associated with N_2 chemisorption while destabilizing the electron depletion associated with O_t chemisorption.

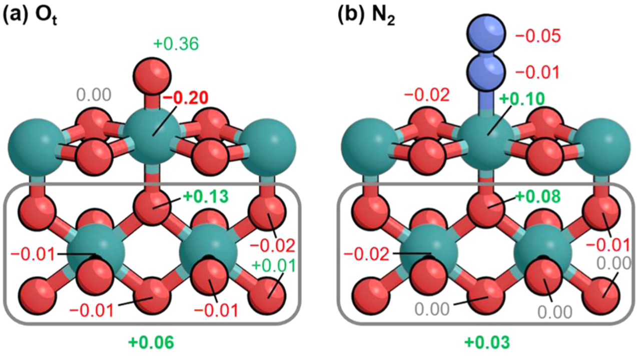

Figure 8. Changes in atomic electron occupancies induced by chemisorption of (a) O_t and (b) N_2 on $RuO_2(110)$. The gray box illustrates the total occupancy (0.06 for O_t and 0.03 for N_2) on the two M_{subcus} atoms and their ten O ligands. Similar occupancy analyses are shown in Figure S6 of the SI for adsorptions onto IrO_2. Blue-green atoms represent Ru, light blue atoms represent N, and red atoms represent O.

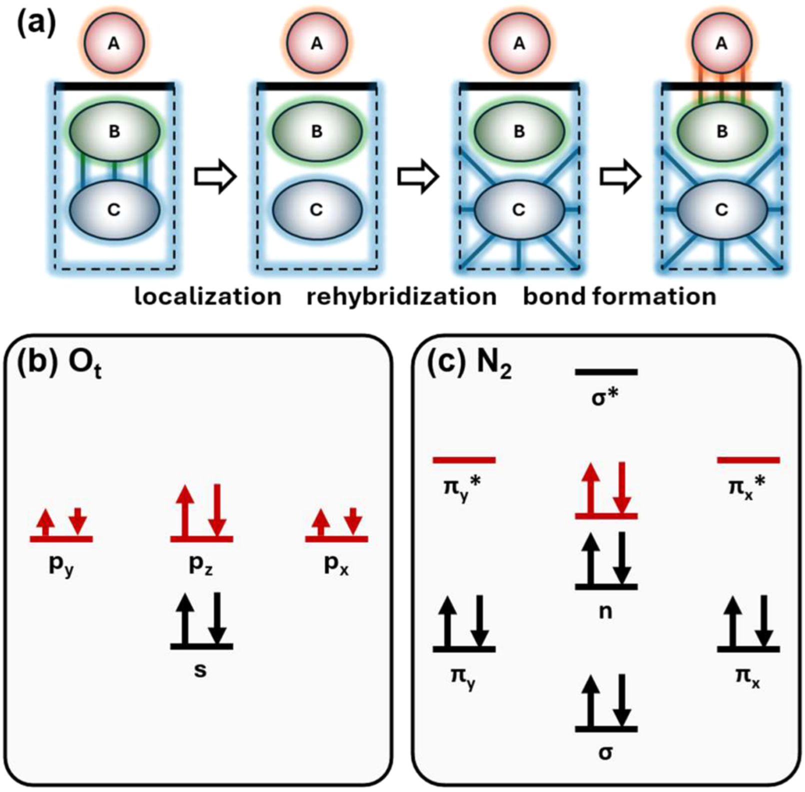

Figure 9. (a) Illustration of how entanglement between orbitals in Sets A, B, and C is decomposed in order to split the charge transfer associated with chemisorption into contributions from localization, rehybridization, and bond formation. Lines represent entanglement between sets of orbitals. Reference states used for (b) O_t and (c) N_2, with the orbitals in Set A shown in red. For O_t, the average of two reference states was used so that the p_y and p_x orbitals each contain half an electron of each spin.

The positive element effect associated with the subsurface metal ligands (M_{subcus}), whereby both adsorbates bind stronger to an adsorption site having subsurface Ir compared to one with subsurface Ru, is less obvious because both adsorptions result in decreases in electron density on these metal atoms of about 0.02 e (which by itself would cause a negative element effect). However, the potential at the ionic core of the subsurface metal atoms is not only determined by the partial charge on the atom itself, but also by the surrounding oxygen atoms (due to interatomic electrostatic interactions). In particular, the subsurface oxygen (O_{sub}) experiences an increase in electron density upon chemisorption (0.13 e for O_t, 0.08 for N_2) that is significantly greater than the decrease on the subsurface metal atoms and all of their other oxygen ligands. If we consider the change in total electron density on the M_2O_{10} cluster (these two metals and their oxygen ligands, gray box in Figure 8), O_t chemisorption leads to a net increase of 0.06 e while N_2 leads to a net increase of 0.03 e. Thus, the electrostatic potential of both Ru_{subcus} and Ir_{subcus} are expected to decrease, because of the increase of electron density on the O_{sub} ligand, leading to a positive element effect for these two subsurface metals.

Decomposing Charge Perturbations upon Adsorption. Having established that the element effect is related to the adsorption-induced change in electron occupancy at the relevant metal atom, we now seek to understand why the two adsorbates have similar effects on the occupancy of the subsurface oxygen (O_{sub}) while having opposite effects on the electron occupancy of the adsorption site (M_{cus}). To do this, we decompose the charge perturbations induced by chemisorption into three bonding channels (σ, π_y, π_x) as well as into distinct processes.

Each bonding channel (σ, π_y, π_x) in the adsorbed state (Figure 9a, right) can be characterized with an adsorbate orbital (collectively referred to as Set A) entangled with a surface orbital (Set B). In the desorbed state (Figure 9a, left), the surface orbitals in Set B are instead entangled with a second set of surface orbitals (Set C). For O_t, the orbitals in Set A consist of an sp_z hybrid, p_y, and p_x, respectively, while for N_2 these are an sp_z lone pair on N along with the two π^* orbitals. To define changes in orbital occupancies within these sets upon adsorption, we use the orbital occupancies of atomic O (Figure 9b) and molecular N_2 (Figure 9c) as references. Because atomic O is an open-shell species, we use the average of two closed-shell reference states, a π-donor reference (with filled p_x and p_y orbitals) and a π-acceptor reference (empty p_x and p_y).

After identifying the surface orbitals in each set, the chemisorption process is split into four steps (three depicted in Figure 9a) in order to decompose the associated charge perturbations. The first step of the decomposition occurs in the surface prior to adsorption and involves disentangling Set B (surface orbitals that will eventually entangle with the adsorbate) from Set C. This disentanglement can be understood as the *localization* of a single electron or hole into each of the orbitals in Set B (Figure 9a). Next, the surface orbitals in Set C undergo *rehybridization* in response to their disentanglement from Set B. Upon adsorption, *bond formation* occurs by the entanglement of the relevant adsorbate orbitals (Set A) with the surface orbitals in Set B. We also include a

	bond	loc	bond+loc
σ	0.39	-0.41	-0.02
π_y	-0.23	-0.45	-0.68
π_x	-0.23	-0.39	-0.62
nb	0.03		0.03
sum	-0.05	-1.24	-1.29
rehyb			0.14
pol			0.95
tot			-0.20

	bond	loc	bond+loc
σ	0.21	-0.12	0.10
π_y	-0.09	0.21	0.12
π_x	-0.09	0.10	0.01
nb	0.00		0.00
sum	0.04	0.19	0.23
rehyb			-0.12
pol			-0.01
tot			0.10

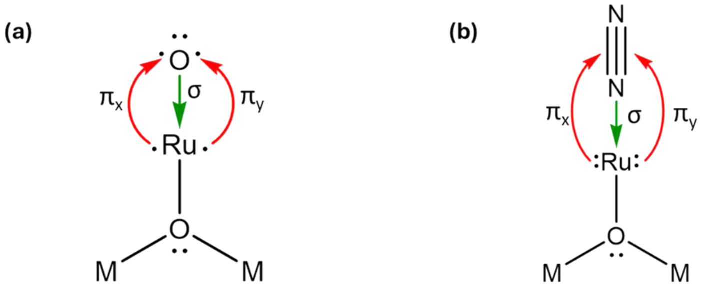

	bond	loc	bond+loc
σ	0.07	0.17	0.24
π_y	-0.05	0.02	-0.03
π_x	-0.01	-0.01	-0.02
nb	0.00		0.00
sum	0.01	0.18	0.19
rehyb			-0.01
pol			-0.04
tot			0.13

	bond	loc	bond+loc
σ	0.05	0.07	0.12
π_y	0.00	0.03	0.03
π_x	0.00	0.01	0.00
nb	0.00		0.00
sum	0.05	0.10	0.15
rehyb			0.02
pol			-0.08
tot			0.08

Figure 10. Decomposition of changes in partial atomic charges on (top) M_{cus} and (bottom) O_{sub} occurring during chemisorption of (a) O_t and (b) N_2 on RuO_2, where positive vs negative values indicate an increase vs decrease in electron density. A similar decomposition is shown in Figure S7 of the SI for adsorption onto IrO_2.

final *polarization* step that accounts for electrostatic screening of the charge perturbations induced by the electronic transformations.

The charge perturbations (changes in electronic occupancies) calculated for each of these transformations are reported in Figure 10 for adsorption of O_t and N_2 on the RuO_2 surface (and in Figure S7 of the SI for adsorption onto IrO_2). Trends in atomic partial charge perturbations induced by chemisorption (sum in Figure 10) are well represented by the combination of localization and bond formation (bond+loc in Figure 10), with the rehybridization and polarization processes serving primarily to attenuate these perturbations. We will therefore focus our discussion on localization and bond formation processes.

For both adsorbates, charge transfer between the surface and adsorbate flows in opposite directions in the σ and π systems, with charge transfer from the adsorbate to the surface in the σ system and charge transfer from the surface to the adsorbate in the π system. These roughly cancel out on both adsorbates, although the π interaction slightly dominates during O_t chemisorption (such that O_t is electron withdrawing, Figure 8a) while the σ interaction slightly dominates during N_2 chemisorption (such that N_2 is electron donating, Figure 8b). The direction of σ charge transfer from the adsorbate to the surface is not surprising since both adsorbates possess a σ lone pair in their reference states (Figure 9) that donates into an unoccupied surface orbital. The π charge transfer from the surface to N_2 can be rationalized as donation from occupied surface orbitals into the unoccupied π^* orbitals of N_2. Because of the relatively high energy of the π^* acceptor orbitals, this interaction is weaker than the σ interaction, explaining why the latter dominates to make N_2 a net electron donor. Additionally, while a small amount of donation occurs from the occupied π orbitals on N_2, it is insignificant due to the low energy of these orbitals compared to the σ lone pair. The π interaction during O_t chemisorption is more complicated because the p_y and p_x orbitals on O_t are half-occupied in the reference state. The p_y and p_x acceptor orbitals on O_t are significantly lower in energy than the π^* orbitals on N_2 and higher in energy than the π orbitals on N_2, making O_t both a better π donor and acceptor. Overall, the withdrawal is significantly stronger than the donation since it counteracts donation from the σ lone pair while complementing the high electronegativity of O_t. We can also see that π withdrawal is stronger than the σ donation, making O_t a net electron acceptor.

Perhaps unexpectedly, the largest contribution to the atomic partial charge perturbations arises from the localization step where the surface orbitals in Set B first disentangle from the

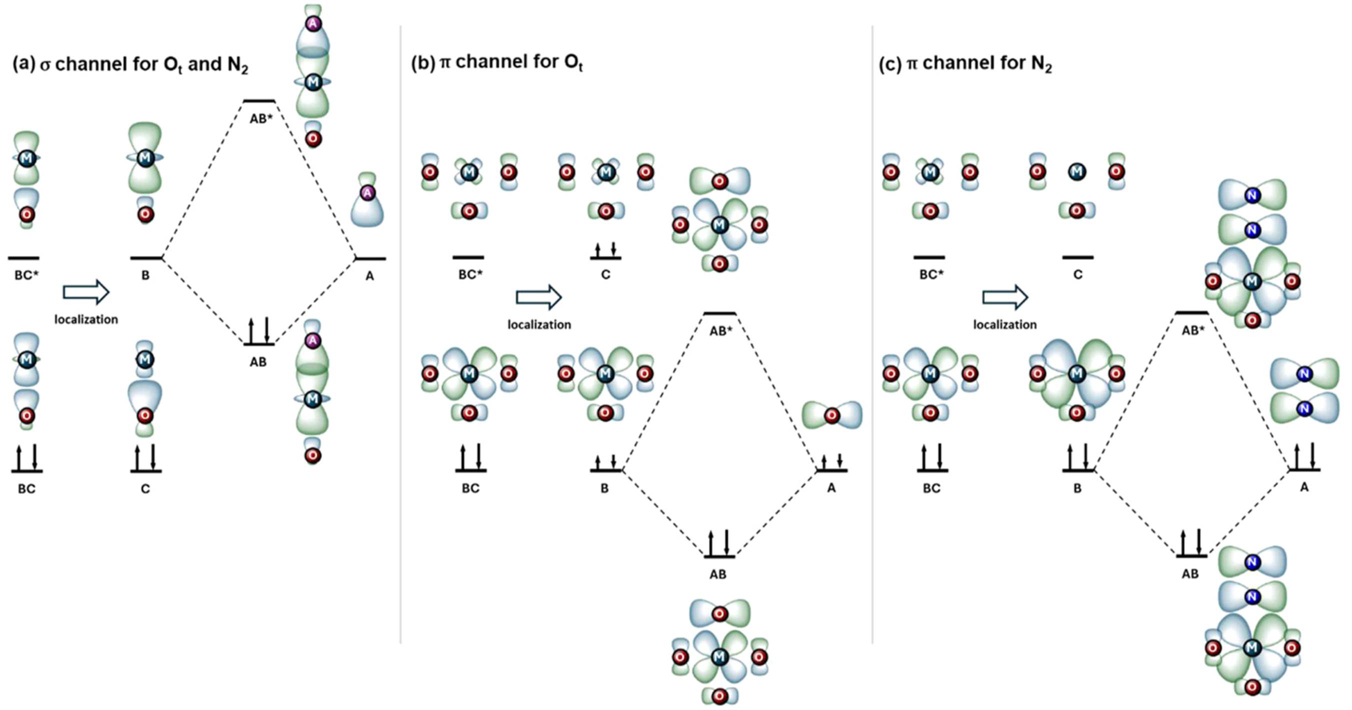

Figure 11. Illustration of orbital transformations involved in localization of (a) the σ system of N_2 or O_t, (b) the π system for O_t, and (c) the π system for N_2. M_{cus} and O_{sub} atoms are shown in all three parts, and surface O ligands are shown in parts (b) and (c). Note that orbitals A, B, and C in part (b) are occupied with half an electron of each spin.

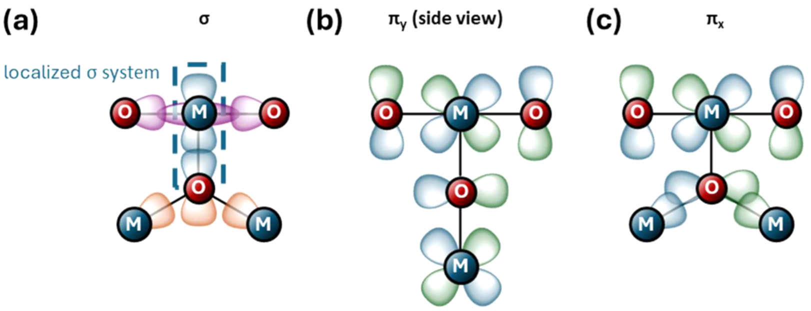

Figure 12. Depiction of orbital overlap in the vicinity of the chemisorption site. (a) In the σ system, the axial sd^n hybrid on M_{cus} and the upward-pointing sp^n hybrid on O_{sub} (light blue) do not have substantial overlap with orbitals on the surface O ligands (magenta) or the subsurface metal cations (orange). This results in a localized σ system on M_{cus} and O_{sub} (dashed blue box) that bonds to the adsorbate. In the (b) π_y and (c) π_x systems, the d_{yz}/d_{xz} orbitals on M_{cus} have overlap with both surface and subsurface O ligands, while the p_y/p_x orbitals on O_{sub} have overlap with M_{cus} as well as the two M_{subcus} cations.

rest of the surface (Set C) prior to entangling with the adsorbate. Each surface orbital in Set B that entangles with the adsorbate in the final state is initially entangled with a surface orbital in Set C. The orbitals form an occupied in-phase combination BC and an unoccupied out-of-phase combination BC*, and localization occurs by hybridization of BC with BC* to end up with unentangled B and C (Figure 11a, left).

If orbital B is an acceptor orbital, as is the case for the σ interaction with both adsorbates (Figure 11a), then the unoccupied BC* transforms into the unoccupied B during localization. In this case, B will have a higher amplitude on M_{cus} than BC* in order to maximize overlap with the σ donor orbital on the adsorbate. At the same time, the occupied BC transforms into the occupied C, with the latter having lower amplitude on M_{cus} than the former. This leads to depletion of electron density on M_{cus}, as is seen for the σ channels in the localization step for both adsorbates (−0.41 for O_t and −0.12 for N_2 in Figure 10). Essentially, Pauli repulsion from the electrons donated from the adsorbate to the metal adsorption site partially displaces the electrons that were originally on the metal site. If instead, orbital B is a donor orbital, as is the case for the π interaction with N_2, then the occupied BC transforms into the occupied B during localization (Figure 11c). Since B has a higher amplitude on M_{cus} than BC, localization leads to accumulation of electron density on M_{cus}.

During localization associated with the π interactions with O_t, the BC→B and BC*→C transformations do not result in a significant change in orbital shape (Figure 11b). Nonetheless, localization also involves the transfer of half an electron of each spin from occupied B to unoccupied C in order for B to entangle with the half-occupied p_y and p_x orbitals on O_t. Because B has a significantly greater magnitude on M_{cus} than C, this results in depletion of electron density on this atom

(−0.45 and −0.39 for π_y and π_x, respectively, Figure 10) during the localization step of O_t adsorption.

Unique Role of Subsurface O and Metal Cations. We now turn to the origin of the significant positive element effect of M_{subcus} and why it is unique to certain metal oxides. As was discussed, this results from an accumulation of electron density on O_{sub} upon adsorption, which is electrostatically stabilized when the positive charge of the ionic core on M_{subcus} increases as Ru is exchanged with Ir. According to the variations in partial atomic occupancies reported in Figure 10, this electron accumulation is associated with charge transfer to and localization of the unoccupied σ acceptor orbital. This results in an accumulation of 0.24 e on O_{sub} during O_t chemisorption and an accumulation of 0.12 e during N_2 chemisorption in σ orbitals, consistent with the greater magnitude of the M_{subcus} element effect on the former compared to the latter (Table 1). For both adsorbates, this accumulation arises both from charge transfer from the adsorbate lone pair to the unoccupied surface orbital as well as from localization of this orbital onto M_{cus}.

While the electron accumulation during bond formation is self-explanatory, the accumulation resulting from localization is less obvious. As shown in Figure 11a, it results from localization of the occupied BC orbital onto O_{sub} (as it transforms to orbital C) at the same time as the unoccupied BC* orbital localizes onto M_{cus} (as it transforms to orbital B). This can be interpreted as Pauli repulsion from the donated adsorbate lone pair pushing electron density from M_{cus} onto O_{sub} via polarization of the M_{cus}−O_{sub} σ bond. As depicted in Figure 12a, the M_{cus}−O_{sub} σ bond mainly involves an axial sd^n hybrid on M_{cus} and an upward-pointing sp^n hybrid on O_{sub}. Due to their directional nature, these two orbitals are only weakly involved in the other bonding interactions of M_{cus} and O_{sub} in the surface that predominantly involve the equatorial sd^n hybrid on M_{cus} and the downward-pointing sp^n hybrid on O_{sub}. This implies that the M_{cus}−O_{sub} bond is fairly localized on M_{cus} and O_{sub} so that the redistribution of electron density occurring during localization is concentrated on these two atoms. This explains the relatively large electron accumulation on O_{sub} during localization, which is analogous to the trans effect observed in coordination complex chemistry.[62]

In contrast to the σ system, the π system is far more delocalized. If we define the degree of localization as the combined fraction $f_{loc} = \frac{1}{4}(n_B + n_C)$, where n_B and n_C reflect the occupancies of orbitals B and C that reside on M_{cus} and O_{sub}, we can see that while the σ system is 61% localized, the π_y and π_x systems are only 38 and 33% localized. As depicted in Figure 12b,c, this is a consequence of only single orbitals on M_{cus} and O_{sub} contributing to each π system (d_{yz}/d_{xz} on M_{subcus} and p_y/p_x on O_{sub} for the π_y/π_x systems, respectively) so that the same orbitals involved in π bonds between O_{sub}, M_{cus}, and the adsorbate are also involved in bonding to M_{subcus} and the surface O ligands. As a result, localization in the π systems leads to electron flow between M_{cus} and multiple atoms, rather than being focused on O_{sub}, precluding a significant contribution to the ligand effects.

A localized M_{cus}−O_{sub} σ bond can exist at metal oxide surfaces in which the O atoms bond to four or fewer metal centers in the bulk and will thus occur for many metal oxide structures. In such structures, a unique sp^n hybrid can be formally associated with each of the O−M bonds so that no two bonds share a single oxygen orbital. In metals, no such electronic separation exists between the different M−M bonds so that the σ bonding is delocalized. We expect this to be a general trend that should result in a significant positive M_{subcus} element effect for any adsorbate that can be considered a σ donor.

DISCUSSION

The site and ligand effects identified in this work can provide opportunities for tuning the catalytic properties of IrO_2/RuO_2(110) mixed-metal oxides, particularly because nearly conformal single layer oxides can be grown in this system. For example, the difference in O_t binding strength (~25 kJ/mol) causes a difference of several orders of magnitude in the O_2 desorption rate from the 1L vs nL oxides, and could significantly alter the energy barriers of catalytic oxidation reactions as well, allowing catalytic properties to be modified by synthesizing 1L vs nL IrO_2/RuO_2 heterostructures. Additionally, differences in binding energy could drive adsorbate interchange among coexisting surface oxide domains (e.g., between 1L-IrO_2 islands and the RuO_2 substrate), potentially giving rise to catalytic behavior that differs from that obtained on uniform oxide surfaces. Atomically dispersed, solid solutions ($Ir_xRu_{1-x}O_2$) could also produce site ensembles with variable chemical properties, though further study is needed to assess how the local environment influences adsorbate binding on $Ir_xRu_{1-x}O_2$(110) surfaces of varying composition. Significantly, our results show that the layered IrO_2/RuO_2 heterostructures undergo negligible mixing at the temperatures needed to promote catalytic chemistry (~450−650 K) on these oxides.[45−47,57,65,66] This stability suggests that the oxide structures will be preserved under catalytic conditions, and thus that catalytic properties can be modified by synthesizing various layered IrO_2/RuO_2 heterostructures.

Our results also demonstrate a computational framework that can explain the origin of element effects for adsorbate binding on materials with both localized and delocalized bonding. This development is significant because it can provide a unified description of both site and ligand element effects on adsorption properties for a wide range of catalytic materials. By using the framework of computational alchemy, one simply needs to rationalize the direction of charge flow between atoms during chemisorption in order to explain these effects. As such, there is no need to explicitly decompose the energetic changes associated with chemisorption, which is a considerably more difficult task. Indeed, our analysis shows that the strong influence of M_{subcus} cations originates from the localized nature of the σ bond between O_{sub} and M_{cus}, an effect that is distinct for these rutile oxide surfaces compared with metals. The computational alchemy framework also explains the opposing site and ligand effects identified for the binding of oxygen on M_{cus} sites of these oxides, further demonstrating its utility. Future work could apply this framework to explain the origin of site and ligand effects on metal surfaces and for different classes of adsorbates to determine if the conclusions presented here are more broadly applicable.

SUMMARY

The binding of N_2 and O_t atoms was investigated on single-layer IrO_2 films on RuO_2(110), single-layer RuO_2 films on IrO_2(110) and their thick-film counterparts grown epitaxially in UHV. TPD measurements show that the binding energies of N_2 and O_t atoms are lower on 1L vs nL-IrO_2/RuO_2 films by ~11 and 25 kJ mol^{-1}, but higher on 1L vs nL-RuO_2/IrO_2 by the same amounts, demonstrating that the identity of the oxide in the second layer has a significant influence on adsorbate binding. DFT calculations and electronic structure analysis corroborate these trends, and show that the binding properties of the M_{cus} sites are mainly determined by the identity of the M_{cus} site and the two M_{subcus} cations beneath the binding site, with other nearby cations having less impact. Our results demonstrate that M_{subcus} cations have a positive element effect on the binding of both N_2 and O_t atoms on M_{cus} sites, such that increasing the valence (i.e., ionic core charge) of the M_{subcus} cations enhances binding. The M_{cus} binding site also has a positive element effect on N_2 binding, but a negative element effect on O_t binding, demonstrating that the M_{cus} and M_{subcus} atoms have similar vs opposite element effects on N_2 and O_t binding, respectively. A framework based on computational alchemy and entanglement decomposition rationalizes both the site and ligand effects observed for these adsorbed species, showing that the positive element effect of the M_{subcus} atoms originates from the adsorbate lone pair pushing electrons in the $M_{cus}-O_{sub}$ σ bond from M_{cus} onto O_{sub} due to Pauli repulsion. This interaction is found to be particularly strong owing to the localized nature of the $M_{cus}-O_{sub}$ σ bond that largely confines electron redistribution in the σ-system to these two atoms. The increase in positive ionic core charge upon replacing Ru with Ir at the M_{subcus} sites electrostatically stabilizes the electron accumulation on O_{sub}, thereby strengthening the binding of both N_2 and O with the M_{cus} site. Overall, our results provide a new framework for understanding site and ligand effects in chemical binding on metal oxides, and suggest possibilities for modifying catalytic properties with layered IrO_2/RuO_2 heterostructures.

■ ASSOCIATED CONTENT

Supporting Information

The Supporting Information is available free of charge at https://pubs.acs.org/doi/10.1021/acscatal.5c02708.

> Experimental Details; estimating the IrO_2 and RuO_2 coverages; TPD analysis to estimate N_2 and O_t binding energies; computational details; DFT calculations for N_2 and O_t binding energies on mixtures; quasi-atomic orbital (QO) calculations; method for decomposing charge flow during chemisorption; charge transfer decomposition results for the IrO_2 surface; atomic occupancies of individual orbitals; comparison with charge transfer values computed using the Bader approach (PDF)

■ AUTHOR INFORMATION

Corresponding Authors

Craig Plaisance − *Cain Department of Chemical Engineering, Louisiana State University, Baton Rouge, Louisiana 70803, United States*; Email: plaisance@lsu.edu

David Hibbitts − *Department of Chemical Engineering, University of Florida, Gainesville, Florida 32611, United States; Davidson School of Chemical Engineering, Purdue University, West Lafayette, Illinois 47907, United States*; orcid.org/0000-0001-8606-7000; Email: hibbitts@purdue.edu

Jason F. Weaver − *Department of Chemical Engineering, University of Florida, Gainesville, Florida 32611, United States*; orcid.org/0000-0002-6777-4727; Email: weaver@che.ufl.edu

Authors

Suriya Ramasubramanian − *Department of Chemical Engineering, University of Florida, Gainesville, Florida 32611, United States*

Jisu Shin − *Department of Chemical Engineering, University of Florida, Gainesville, Florida 32611, United States*

Christopher J. Lee − *Department of Chemical Engineering, University of Florida, Gainesville, Florida 32611, United States*; orcid.org/0000-0002-8703-8209

Chethana Sudarshan − *Department of Chemical Engineering, University of Florida, Gainesville, Florida 32611, United States*

Omar Almarshad − *Department of Chemical Engineering, University of Florida, Gainesville, Florida 32611, United States*

Alvaro Loaiza Orduz − *Cain Department of Chemical Engineering, Louisiana State University, Baton Rouge, Louisiana 70803, United States*

Randall J. Meyer − *ExxonMobil Technology and Engineering, Annandale, New Jersey 08801, United States*; orcid.org/0000-0002-0679-0029

Complete contact information is available at: https://pubs.acs.org/10.1021/acscatal.5c02708

Notes

The authors declare no competing financial interest.

■ ACKNOWLEDGMENTS

S.R., J.S., D.H., and J.F.W. acknowledge support from the National Science Foundation (NSF CHEM #2102211). A.L.O. and C.P. acknowledge support from the National Science Foundation (NSF CHEM #1954611). R.J.M., C.J.L., O.A., D.H., and J.F.W. acknowledge support from ExxonMobil Technology and Engineering. Computational resources were provided by the University of Florida Research Computing. Portions of this research were conducted with high performance computing resources provided by Louisiana State University (http://www.hpc.lsu.edu).

■ REFERENCES

(1) Hannagan, R. T.; Giannakakis, G.; Flytzani-Stephanopoulos, M.; Sykes, E. C. H. Single-atom alloy catalysts. *Chem. Rev.* **2020**, *120* (1), 12044−12088.

(2) Guan, E. J.; Ciston, J.; Bare, S. R.; Runnebaum, R. C.; Katz, A.; Kulkarni, A.; Kronawitter, C. X.; Gates, B. C. Supported Metal Pair-Site Catalysts. *ACS Catal.* **2020**, *10* (16), 9065−9085.

(3) Gates, B. C.; Flytzani-Stephanopoulos, M.; Dixon, D. A.; Katz, A. Atomically dispersed supported metal catalysts: perspectives and suggestions for future research. *Catal. Sci. Technol.* **2017**, *7* (19), 4259−4275.

(4) Kitchin, J. R.; Norskov, J. K.; Barteau, M. A.; Chen, J. G. Role of strain and ligand effects in the modification of the electronic and chemical properties of bimetallic surfaces. *Phys. Rev. Lett.* **2004**, *93* (15), No. 156801.

(5) Kitchin, J. R.; Norskov, J. K.; Barteau, M. A.; Chen, J. G. Modification of the surface electronic and chemical properties of Pt(111) by subsurface 3d transition metals. *J. Chem. Phys.* **2004**, *120* (21), 10240−10246.

(6) Nilekar, A. U.; Alayoglu, S.; Eichhorn, B.; Mavrikakis, M. Preferential CO Oxidation in Hydrogen: Reactivity of Core-Shell Nanoparticles. *J. Am. Chem. Soc.* **2010**, *132* (21), 7418−7428.

(7) Schaal, M. T.; Hyman, M. P.; Rangan, M.; Ma, S.; Williams, C. T.; Monnier, J. R.; Medlin, J. W. Theoretical and experimental studies of Ag-Pt interactions for supported Ag-Pt bimetallic catalysts. *Surf. Sci.* **2009**, *603* (4), 690−696.

(8) Montemore, M. M.; Medlin, J. W. Predicting and Comparing C-M and O-M Bond Strengths for Adsorption on Transition Metal Surfaces. *J. Phys. Chem. C* **2014**, *118* (5), 2666−2672.

(9) Rodriguez, J. A.; Campbell, R. A.; Goodman, D. W. The Nature of Metal-Metal Bonding at Bimetallic Interfaces. *Surf. Sci.* **1994**, *307*−*309*, 377−383.

(10) Pallassana, V.; Neurock, M.; Hansen, L. B.; Hammer, B.; Norskov, J. K. Theoretical analysis of hydrogen chemisorption on Pd(111), Re(0001) and Pd-ML/Re(0001), Re-ML/Pd(111) pseudomorphic overlayers. *Phys. Rev. B* **1999**, *60* (8), 6146−6154.

(11) Greiner, M. T.; Jones, T. E.; Beeg, S.; Zwiener, L.; Scherzer, M.; Girgsdies, F.; Piccinin, S.; Armbruster, M.; Knop-Gericke, A.; Schlogl, R. Free-atom-like d states in single-atom alloy catalysts. *Nat. Chem.* **2018**, *10* (10), 1008−1015.

(12) Wegener, E. C.; Bukowski, B. C.; Yang, D. L.; Wu, Z. W.; Kropf, A. J.; Delgass, W. N.; Greeley, J.; Zhang, G. H.; Miller, J. T. Intermetallic Compounds as an Alternative to Single-atom Alloy Catalysts: Geometric and Electronic Structures from Advanced X-ray Spectroscopies and Computational Studies. *ChemCatChem* **2020**, *12* (5), 1325−1333.

(13) Dasgupta, A.; Rioux, R. M. Intermetallics in catalysis: An exciting subset of multimetallic catalysts. *Catal. Today* **2019**, *330*, 2−15.

(14) Stacchiola, D. J.; Senanayake, S. D.; Liu, P.; Rodriguez, J. A. Fundamental Studies of Well-Defined Surfaces of Mixed-Metal Oxides: Special Properties of MO_x/TiO_2(110) {M = V, Ru, Ce, or W}. *Chem. Rev.* **2013**, *113* (6), 4373−4390.

(15) Mehar, V.; Kim, M.; Shipilin, M.; Van den Bossche, M.; Gustafson, J.; Merte, L. R.; Hejral, U.; Gronbeck, H.; Lundgren, E.; Asthagiri, A.; Weaver, J. F. Understanding the intrinsic surface reactivity of single-layer and multilayer PdO(101) on Pd(100). *ACS Catal.* **2018**, *8* (9), 8553−8567.

(16) Merte, L. R.; Heard, C. J.; Zhang, F.; Choi, J.; Shipilin, M.; Gustafson, J.; Weaver, J. F.; Gronbeck, H.; Lundgren, E. Tuning the Reactivity of Ultrathin Oxides: NO Adsorption on Monolayer FeO(111). *Angew. Chem., Int. Ed.* **2016**, *55* (32), 9267−9271.

(17) Martin, N. M.; van den Bossche, M.; Hellman, A.; Gronbeck, H.; Hakanoglu, C.; Gustafson, J.; Blomberg, S.; Johanson, N.; Liu, Z.; Axnanda, S.; Weaver, J. F.; Lundgren, E. Intrinsic ligand effect governing the catalytic activity of Pd oxide thin films. *ACS Catal.* **2014**, *4*, 3330−3334.

(18) Fung, V.; Hu, G. X.; Tao, F.; Jiang, D. E. Methane Chemisorption on Oxide-Supported Pt Single Atom. *ChemPhysChem* **2019**, *20* (17), 2217−2220.

(19) Fung, V.; Tao, F.; Jiang, D. E. Low-temperature activation of methane on doped single atoms: descriptor and prediction. *Phys. Chem. Chem. Phys.* **2018**, *20* (35), 22909−22914.

(20) McFarland, E. W.; Metiu, H. Catalysis by Doped Oxides. *Chem. Rev.* **2013**, *113* (6), 4391−4427.

(21) Krcha, M. D.; Mayernick, A. D.; Janik, M. J. Periodic trends of oxygen vacancy formation and C-H bond activation over transition metal-doped CeO2 (111) surfaces. *J. Catal.* **2012**, *293*, 103−115.

(22) Albarracin-Suazo, S.; Freitas, L. F. D. E.; MacQueen, B.; Heyden, A.; Lauterbach, J. A.; Nikolla, E.; Pagán-Torres, Y. J. Supported Bifunctional Molybdenum Oxide-Palladium Catalysts for Selective Hydrodeoxygenation of Biomass-Derived Polyols and 1,4-Anhydroerythritol. *ACS Sustainable Chem. Eng.* **2022**, *10* (18), 5719−5727.

(23) Li, Y. C.; Cheng, D. F.; Wei, Z. Y.; Sautet, P. Photoelectron Storage at the WO_3/TiO_2 Interface: Modeling in Ambient Conditions from First-Principles Calculations. *ACS Catal.* **2023**, *13* (15), 9979−9986.

(24) Mamedov, K.; Shrestha, A.; Whitcomb, C. A.; Paolucci, C.; Davis, R. J. Influence of Domain Size and Support Composition on the Reducibility of SiO_2 and TiO_2 Supported Tungsten Oxide Clusters. *J. Phys. Chem. C* **2024**, *128* (33), 13864−13878.

(25) Over, H. Surface chemistry of ruthenium dioxide in heterogeneous catalysis and electrocatalysis: From fundamental to applied research. *Chem. Rev.* **2012**, *112* (6), 3356−3426.

(26) Weaver, J. F. Surface chemistry of late transition metal oxides. *Chem. Rev.* **2013**, *113*, 4164−4215.

(27) Abb, M. J. S.; Herd, B.; Over, H. Template-assisted growth of ultrathin single-crystalline IrO_2(110) films on RuO_2(110)/Ru(0001) and its thermal stability. *J. Phys. Chem. C* **2018**, *122* (26), 14725−14732.

(28) Martin, R.; Kim, M.; Lee, C. J.; Shariff, M. S.; Feng, F.; Meyer, R. J.; Asthagiri, A.; Weaver, J. F. Molecular chemisorption of N_2 on IrO_2(110). *J. Chem. Phys.* **2020**, *152* (7), No. 074712.

(29) Mcdaniel, C. L.; Schneider, S. J. Phase Relations in Ru-Ir-O_2 System in Air. *J. Res. Natl. Bur. Stand. A., Phys. Chem.* **1969**, *A 73* (2), 213 DOI: 10.6028/jres.073A.019.

(30) Chaudhary, P.; Zagalskaya, A.; Over, H.; Alexandrov, V. Strain-Dependent Activity-Stability Relations in RuO_2 and IrO_2 Oxygen Evolution Catalysts. *Chemelectrochem* **2024**, *11* (1), No. e202300659.

(31) Song, J. J.; Wei, C.; Huang, Z. F.; Liu, C. T.; Zeng, L.; Wang, X.; Xu, Z. C. J. A review on fundamentals for designing oxygen evolution electrocatalysts. *Chem. Soc. Rev.* **2020**, *49* (7), 2196−2214.

(32) Chen, F. Y.; Wu, Z. Y.; Adler, Z.; Wang, H. T. Stability challenges of electrocatalytic oxygen evolution reaction: From mechanistic understanding to reactor design. *Joule* **2021**, *5* (7), 1704−1731.

(33) Ma, Z.; Zhang, Y.; Liu, S. Z.; Xu, W. Q.; Wu, L. J.; Hsieh, Y. C.; Liu, P.; Zhu, Y. M.; Sasaki, K.; Renner, J. N.; Ayers, K. E.; Adzic, R. R.; Wang, J. X. Reaction mechanism for oxygen evolution on RuO_2, IrO_2, and RuO_2@IrO_2 core-shell nanocatalysts. *J. Electroanal. Chem.* **2018**, *819*, 296−305.

(34) Kasian, O.; Geiger, S.; Stock, P.; Polymeros, G.; Breitbach, B.; Savan, A.; Ludwig, A.; Cherevko, S.; Mayrhofer, K. J. J. On the Origin of the Improved Ruthenium Stability in RuO_2-IrO_2 Mixed Oxides. *J. Electrochem. Soc.* **2016**, *163* (11), F3099−F3104.

(35) Gu, X. K.; Camayang, J. C. A.; Samira, S.; Nikolla, E. Oxygen evolution electrocatalysis using mixed metal oxides under acidic conditions: Challenges and opportunities. *J. Catal.* **2020**, *388*, 130−140.

(36) Dickens, C. F.; Kirk, C.; Norskov, J. K. Insights into the Electrochemical Oxygen Evolution Reaction with ab Initio Calculations and Microkinetic Modeling: Beyond the Limiting Potential Volcano. *J. Phys. Chem. C* **2019**, *123* (31), 18960−18977.

(37) Li, J.; Tian, W. C.; Li, Q.; Zhao, S. L. Acidic Oxygen Evolution Reaction: Fundamental Understanding and Electrocatalysts Design. *ChemSusChem* **2024**, *17* (15), No. e202400239.

(38) Ying, J.; Chen, J. B.; Xiao, Y. X.; de Torresi, S. I. C.; Ozoemena, K. I.; Yang, X. Y. Recent advances in Ru-based electrocatalysts for oxygen evolution reaction. *J. Mater. Chem. A* **2023**, *11* (4), 1634−1650.

(39) Vazhayil, A.; Vazhayal, L.; Thomas, J.; Ashok, C. S.; Thomas, N. A comprehensive review on the recent developments in transition metal-based electrocatalysts for oxygen evolution reaction. *Appl. Surf. Sci. Adv.* **2021**, *6*, No. 100184.

(40) Owe, L. E.; Tsypkin, M.; Wallwork, K. S.; Haverkamp, R. G.; Sunde, S. Iridium-ruthenium single phase mixed oxides for oxygen evolution: Composition dependence of electrocatalytic activity. *Electrochim. Acta* **2012**, *70*, 158−164.

(41) Li, G. Q.; Li, S. T.; Ge, J. J.; Liu, C. P.; Xing, W. Discontinuously covered IrO_2-RuO_2@Ru electrocatalysts for the oxygen evolution reaction: how high activity and long-term durability can be simultaneously realized in the synergistic and hybrid nanostructure. *J. Mater. Chem. A* **2017**, *5* (33), 17221−17229.

(42) Martin, R.; Kim, M.; Asthagiri, A.; Weaver, J. F. Alkane activation and oxidation on late-transition-metal oxides: Challenges and opportunities. *ACS Catal.* **2021**, *11* (8), 4682−4703.

(43) Bian, Y. X.; Kim, M.; Li, T.; Asthagiri, A.; Weaver, J. F. Facile dehydrogenation of ethane on the IrO_2(110) surface. *J. Am. Chem. Soc.* **2018**, *140* (7), 2665−2672.

(44) Liang, Z.; Li, T.; Kim, M.; Asthagiri, A.; Weaver, J. F. Low-temperature activation of methane on the IrO_2(110) surface. *Science* **2017**, *356* (6335), 299−303.

(45) Jamir, J.; Pope, C.; Ramasubramanian, S.; Mehar, V.; Shi, J. J.; Weaver, J. F. Influence of Water on the Catalytic Oxidation of Ethane on $IrO_2(110)$. *ACS Catal.* **2024**, *14* (9), 7062−7073.

(46) Jamir, J.; Kim, M.; Pope, C.; Asthagiri, A.; Weaver, J. F. Linking operando spectroscopy with microkinetic modeling to unravel the catalytic mechanism for CH_4 oxidation on $IrO_2(110)$. *ACS Catal.* **2023**, *13* (22), 14598−14613.

(47) Khalid, O.; Luciano, A. S.; Drazic, G.; Over, H. Mixed $Ru_xIr_{1-x}O_2$ supported on rutile TiO_2: Catalytic methane combustion, a model study. *ChemCatChem* **2021**, *13* (18), 3983−3994.

(48) Saravanan, K.; Kitchin, J. R.; von Lilienfeld, O. A.; Keith, J. A. Alchemical Predictions for Computational Catalysis: Potential and Limitations. *J. Phys. Chem. Lett.* **2017**, *8* (20), 5002−5007.

(49) Pope, C.; Yun, J.; Reddy, R.; Jamir, J.; Kim, D.; Kim, M.; Asthagiri, A.; Weaver, J. F. Surface chlorination of $IrO_2(110)$ by HCl. *J. Chem. Phys.* **2024**, *161* (6), No. 064704.

(50) Lee, C. J.; Vashishtha, S.; Shariff, M.; Zou, F. R.; Shi, J. J.; Meyer, R. J.; Weaver, J. F. Kinetics and selectivity of methane oxidation on an $IrO_2(110)$ film. *J. Phys.: Condens. Matter* **2022**, *34* (28), No. 284002.

(51) Abb, M. J. S.; Weber, T.; Langsdorf, D.; Koller, V.; Gericke, S. M.; Pfaff, S.; Busch, M.; Zetterberg, J.; Preobrajenski, A.; Gronbeck, H.; Lundgren, E.; Over, H. Thermal stability of single-crystalline $IrO_2(110)$ layers: Spectroscopic and adsorption studies. *J. Phys. Chem. C* **2020**, *124*, 15324−15336.

(52) Wang, C. C.; Siao, S. S.; Jiang, J. C. Density Functional Theory Study of NH_x ($x = 0{-}3$) and N_2 Adsorption on $IrO_2(110)$ Surfaces. *J. Phys. Chem. C* **2010**, *114* (43), 18588−18593.

(53) Kim, Y. D.; Seitsonen, A. P.; Over, H. Adsorption characteristics of CO and N-2 on RuO2(110). *Phys. Rev. B* **2001**, *63* (11), No. 115419.

(54) Li, T.; Kim, M.; Liang, Z.; Asthagiri, A.; Weaver, J. Hydrogen oxidation on oxygen-rich $IrO_2(110)$. *Catal., Struct. React.* **2018**, *4*, 1−13.

(55) Kim, M.; Franklin, A.; Martin, R.; Feng, F.; Li, T.; Liang, Z.; Asthagiri, A.; Weaver, J. Adsorption and oxidation of CH_4 on oxygen-rich $IrO_2(110)$. *J. Phys. Chem. C* **2019**, *123* (45), 27603−27614.

(56) Kim, Y. D.; Seitsonen, A. P.; Wendt, S.; Wang, J.; Fan, C.; Jacobi, K.; Over, H.; Ertl, G. Characterization of various oxygen species on an oxide surface: $RuO_2(110)$. *J. Phys. Chem. B* **2001**, *105* (18), 3752−3758.

(57) Jamir, J.; Yun, J.; Pope, C.; Kim, M.; Asthagiri, A.; Weaver, J. F. Ethane adsorption and oxidation on $IrO_2(110)$ surfaces. *J. Phys. Chem. C* **2024**, *128* (1), 111−122.

(58) Li, T.; Kim, M.; Liang, Z.; Asthagiri, A.; Weaver, J. F. Dissociative chemisorption and oxidation of H_2 on the stoichiometric $IrO_2(110)$ surface. *Top. Catal.* **2018**, *61* (5−6), 397−411.

(59) Pogodin, S.; Lopez, N. A More Accurate Kinetic Monte Carlo Approach to a Monodimensional Surface Reaction: The Interaction of Oxygen with the $RuO_2(110)$ Surface. *ACS Catal.* **2014**, *4* (7), 2328−2332.

(60) Wang, H. Y.; Schneider, W. F. Effects of coverage on the structures, energetics, and electronics of oxygen adsorption on $RuO_2(110)$. *J. Chem. Phys.* **2007**, *127* (6), No. 064706.

(61) Ocampo-Restrepo, V. K.; Vijay, S.; Gunasooriya, G. T. K. K.; Norskov, J. K. Characterization of adsorption sites on IrO_2 temperature programmed O_2 desorption simulations. *Phys. Chem. Chem. Phys.* **2024**, *26* (24), 17396−17404.

(62) Coe, B. J.; Glenwright, S. J. Trans-effects in octahedral transition metal complexes. *Coord. Chem. Rev.* **2000**, *203*, 5−80.

(63) Qian, X. F.; Li, J.; Qi, L.; Wang, C. Z.; Chan, T. L.; Yao, Y. X.; Ho, K. M.; Yip, S. Quasiatomic orbitals for ab initio tight-binding analysis. *Phys. Rev. B* **2008**, *78* (24), No. 245112.

(64) Plaisance, C. P.; van Santen, R. A.; Reuter, K. Constrained-Orbital Density Functional Theory. Computational Method and Applications to Surface Chemical Processes. *J. Chem. Theory Comput.* **2017**, *13* (8), 3561−3574.

(65) Timmer, P.; Over, H. Active Phase of IrO_2 in the Catalytic CH_4 Combustion Reaction: Operando Infrared Spectroscopy and Online Gas Analysis. *J. Phys. Chem. C* **2024**, *128* (3), 1068−1074.

(66) Khalid, O.; Weber, T.; Drazic, G.; Djerdj, I.; Over, H. Mixed RuxIr1-xO2 Oxide Catalyst with Well-Defined and Varying Composition Applied to CO Oxidation. *J. Phys. Chem. C* **2020**, *124* (34), 18670−18683.